



1

2 **Performance of AIRS ozone retrieval over the central Himalayas: Case studies of biomass**  
3 **burning, downward ozone transport and radiative forcing using long-term observations**

4

5

6 Prajwal Rawat<sup>1,5</sup>, Manish Naja<sup>1</sup>, Evan Fishbein<sup>2</sup>, Pradeep K. Thapliyal<sup>3</sup>, Rajesh Kumar<sup>4</sup>, Piyush  
7 Bhardwaj<sup>4</sup>, Aditya Jaiswal<sup>1</sup>, Sugriva N. Tiwari<sup>5</sup>, Sethuraman Venkataramani<sup>6</sup>, Shyam Lal<sup>6</sup>

8

9

10

11 <sup>1</sup> Aryabhata Research Institute of Observational Sciences (ARIES), Nainital, India

12 <sup>2</sup> NASA Jet Propulsion Laboratory, Pasadena, CA 91109, USA

13 <sup>3</sup> Space Applications Centre, ISRO, Ahmedabad 380 015, India

14 <sup>4</sup> National Center for Atmospheric Research (NCAR) Boulder, CO 80307, USA

15 <sup>5</sup> DDU Gorakhpur University, Gorakhpur 273 009, India

16 <sup>6</sup> Physical Research Laboratory (PRL), Ahmedabad, 380009, India

17

18

19

20

21 **Corresponding author:** Manish Naja ([manish@aries.res.in](mailto:manish@aries.res.in))

22

23

24

25



26 **Short Summary:**

27 Satellite based ozone observations have gained wide importance due to their global coverage.  
28 However, satellite retrieved products are less direct and needs to be validated, particularly in  
29 complex terrain region. Here, ozonesonde launched from a Himalayan site is utilized to assess the  
30 Atmospheric Infrared Sounder (AIRS) ozone retrieval. AIRS is shown to overestimates ozone in  
31 the upper troposphere and lower stratosphere but does reasonably well in the lower troposphere  
32 and stratosphere.

33

34

35

36

37

38

39

40

41

42

43

44

45

46

47

48

49

50



51 **Abstract:**

52 Data from ozonesondes launched at ARIES Nainital (29.40° N, 79.50° E, and 1793 m elevation)  
53 are used to evaluate the Atmospheric Infrared Sounder (AIRS) version 6 ozone profiles and total  
54 column ozone during the period 2011-2017 over the central Himalaya. The AIRS ozone products  
55 are analyzed in terms of retrieval sensitivity, retrieval biases/errors, and ability to retrieve the  
56 natural variability of columnar ozone, which has not been done so far from the Himalayan region  
57 having complex topography. For a direct comparison, averaging kernels information is used to  
58 account for the sensitivity difference between the AIRS and ozonesonde data. We show that AIRS  
59 can provide quality data of ozone in the lower and middle troposphere and stratosphere with  
60 nominal underestimation (<20%). However, in the upper troposphere and lower stratosphere  
61 (UTLS), we observe a considerable overestimation of the magnitude as high as 102%. The  
62 weighted statistical error analysis of AIRS ozone shows higher positive bias, root mean squared  
63 error, and standard deviation in the upper troposphere of about 65%, 65%, and 25%, respectively.  
64 Similar to AIRS, Infrared Atmospheric Sounding Interferometer (IASI) and Cross-track Infrared  
65 Sounder (CrIS) are also able to produce ozone peaks and gradients successfully. However, the  
66 statistical errors are again higher in the UTLS region that are likely related to larger variability of  
67 ozone, lower ozone partial pressure and inadequate retrieval information on the surface  
68 parameters. The monthly variations of columnar ozone (total, UTLS, and tropospheric) are  
69 captured well by AIRS, except the total columnar ozone, which shows a strong bimodal variation,  
70 unlike unimodal variation seen in ozonesonde and Ozone Monitoring Instrument (OMI). Increases  
71 in ozone of 5 - 20% (in 2 - 6 km altitude) after the biomass burning and during events of downward  
72 transport (in 2 - 16 km altitude) are captured well by AIRS. Ozone radiative forcing (RF) derived  
73 from total column ozone matches well between ozonesonde (4.86 mW/m<sup>2</sup>) and OMI (4.04  
74 mW/m<sup>2</sup>), while significant RF underestimation is seen in AIRS (2.96 mW/m<sup>2</sup>). The fragile and  
75 complex landscapes of the Himalayas are more sensitive to global climate change, and establishing  
76 such biases and error analysis of space-borne sensors will help study the long-term trends and  
77 estimate accurate radiative budgets.

78  
79  
80  
81



82 **1. Introduction:**

83 Atmospheric ozone is an essential trace gas that plays a crucial role in the atmospheric oxidizing  
84 chemistry, air quality, and earth's radiative budget. The stratospheric ozone absorbs harmful solar  
85 ultraviolet radiation and protects biological life on earth, whereas tropospheric ozone, being a  
86 secondary air pollutant (Pierce et al., 2009) and greenhouse gas, contributes to global warming and  
87 can harm human health and crops when present in higher concentrations near the surface (Fishman  
88 et al., 1979; Ebi and McGregor 2008; Lal et al., 2017). Different radiative forcing of ozone from  
89 the stratosphere (cooling) to the troposphere (heating) (Lacis et al., 1990; Forster et al., 2007;  
90 Wang et al., 1993; Hegglin et al., 2015) demonstrate its potential importance as an atmospheric  
91 climate gas (Shindell et al., 2012). Hence, information regarding precise long-term variability in  
92 global ozone distribution is vital for better characterizing atmospheric chemistry and global  
93 climate changes (McPeters et al., 1997).

94

95 In recent decades, observations of ozone from space-borne sensors (microwave limb sounding,  
96 UV-VIS, and IR) has become an increasingly robust tool for global and higher temporal  
97 monitoring (Fishman et al., 1986; Munro et al., 1998; Foret et al., 2014). This increases our ability  
98 to analyze various influences of human activities on the atmospheric chemical composition  
99 including ozone, study their long-term impact on climate (Fishman et al., 1987), and estimate  
100 reliable radiative budgets (Hauglustaine and Brasseur 2001; Gauss et al., 2003; Aghedo et al.,  
101 2011). However, the space-based sensors are indirect and measure the atmospheric composition  
102 based upon specific algorithms utilizing radiative transfer models and a-priori information. Hence,  
103 the retrieval outputs need to be evaluated with certain reference instruments for establishing the  
104 credibility and better utilization of space-borne data.



105 The Himalayas, a complex terrain region, has the largest abundance of ice sheets outside Polar  
106 regions that impacts global/regional radiative budgets and climate pervasively (e.g., Lawrence and  
107 Lelieveld, 2010; Lelieveld et al., 2018). Here, the in-situ ground-based observations are very  
108 sparse and limited, and complex topography along with inadequate information on the surface  
109 parameters make it difficult to retrieve atmospheric composition from space-borne instruments.  
110 This is because ozone weighting function, a measure of the retrieval sensitivity and a fundamental  
111 retrieval component, depends upon various atmospheric parameters like surface temperature,  
112 surface emissivity, and terrain height (Rodgers et al., 1976, 1990; Bai et al., 2014), which is not  
113 uniform over the foot-print size of the AIRS (~ 13 km x 13 km) over the Himalayas. Usually, the  
114 ozone weighting function has a shorter integrating path over the elevated terrain regions, which  
115 follows a smaller weighting function and provides lesser sensitivity and higher errors in the final  
116 retrievals (Coheur et al., 2005; Bai et al., 2014). Apart from the terrain height, retrieval also  
117 depends on other factors like surface emissivity, atmospheric input constituents, input error  
118 minimizing parameters, etc., whose accuracy matters, alters the retrieval processes abruptly, and  
119 introduces error in the final retrieval.

120

121 The Atmospheric Infrared Sounder (AIRS) onboard the Aqua satellite has been providing reliable  
122 vertical profiles of ozone, temperature, water vapor, and other trace gases globally twice a day  
123 since 2002. Numerous validation studies of AIRS retrieved ozone have been carried out for  
124 different versions since it started operating (2002). For example, Bian et al. (2007) studied AIRS  
125 version 4 over Beijing and discussed the potential agreements (within 10%) between AIRS and  
126 ozonesonde (GPSO3) ozone, particularly in the upper troposphere and lower stratosphere (UTLS)  
127 region with the capability of AIRS to identify various Stratosphere-Troposphere Exchange (STE)



128 and transient convective events. Similarly, a study over Boulder and Lauder by Monahan et al.  
129 (2007) using a similar AIRS version showed despite the larger biases in the lower and middle  
130 tropospheric region, the retrieval algorithm captures the ozone variability very effectively with a  
131 positive correlation of more than 70%. However, that study suggested a need for tropopause-  
132 adjusted coordinates in the a-priori profiles. Both these studies (Bian et al., 2007; Monahan et al.,  
133 2007) show larger biases of AIRS ozone in the lower and middle tropospheric regions, however,  
134 shifts in retrieval biases and errors were seen towards the UTLS region in version 5 (Divakarla et  
135 al., 2008), apart from significant improvements in the lower troposphere. The retrieval  
136 methodology has also changed significantly between V4 and V5. Version 4 or earlier used  
137 regression retrieval as the first guess in physical retrieval while later versions used a climatology-  
138 based first guess for the physical retrieval. Also, radiative transfer models, selected channel sets,  
139 and clarified quality indicators have been modified and improved in all successive versions.

140

141 The AIRS ozone retrieval in V5 and later has improved significantly with retrieval biases and root  
142 mean square error (RMSE) less than 5% and 20%, respectively (Divakarla et al., 2008), over the  
143 tropical regions. However, there is not much discussion and studies of the assessment for AIRS  
144 ozone over the Himalayas' complex terrain, where retrieval is expected to be erroneous due to large  
145 surface variability within its footprint. Also, most of the previous studies (Bian et al., 2006;  
146 Divakarla et al. 2008; Pittman et al., 2009) did not utilize the averaging kernels information of the  
147 AIRS that is vital for satellite evaluation.

148

149 Here, evaluation of AIRS version 6, which entirely depends upon the infra-red (IR) observations  
150 after the failure of the AMSU sensor, is presented in terms of statistical analysis and ability to



151 retrieve the natural variability of ozone at various altitudes over the central Himalayan region using  
152 in-situ ozonesonde observations convolved with AIRS averaging kernels. Additionally, the present  
153 study assessed the AIRS retrieval algorithm using IASI and CrIS radiance information for one  
154 year. AIRS columnar ozone (i.e., total, UTLS, and tropospheric columns) is also assessed with  
155 ozonesonde, OMI, and MLS observations. AIRS has a long-term data set for ozone and  
156 meteorological parameters, establishing such biases and error analysis is essential to make  
157 meaningful use of its data to characterize the Himalayan atmosphere, study the trends, radiative  
158 budgets, perform the model evaluation and data assimilation over this region.

159

## 160 **2 Data and Methodology**

### 161 **2.1 Data Description**

#### 162 **2.1.1 AIRS**

163 Atmospheric Infrared Sounder (AIRS) onboard Aqua satellite, in a sun- synchronous polar orbit  
164 at 705 km altitude, is a hyperspectral thermal infrared grating spectrometer with equatorial  
165 crossings at ~13:30 local time (LT). It is a nadir scanning sensor that was deployed in orbit on  
166 May 4, 2002. AIRS along with its partner microwave instrument, the Advanced Microwave  
167 Sounding Unit (AMSU-A), represents the most advanced atmospheric sounding system placed in  
168 space using cutting-edge infrared and microwave technologies. These instruments together  
169 observe the global energy cycles, water cycles, climate variations, and greenhouse gases, however  
170 after AMSU failure the retrieval now mostly depends upon the AIRS IR observations. The AIRS  
171 infrared spectrometer acquires 2378 spectral samples at resolutions ( $\lambda/\Delta\lambda$ ) ranging from 1086 to  
172  $1570\text{ cm}^{-1}$ , in three bands:  $3.74\text{ }\mu\text{m}$  to  $4.61\text{ }\mu\text{m}$ ,  $6.20\text{ }\mu\text{m}$  to  $8.22\text{ }\mu\text{m}$ , and  $8.8\text{ }\mu\text{m}$  to  $15.4\text{ }\mu\text{m}$   
173 (Fishbein et al., 2003; Pagano et al., 2003). The independent channels of AIRS permit retrieval of



174 various atmospheric states and constituents depending upon their corresponding spectral response  
175 even in the presence of 90% cloud fraction (Susskind et al., 2003; Maddy et al., 2008). In this  
176 study, we have used Level 2 Support physical products of AIRS (AIRS2SUP). The AIRS2SUP  
177 files (~240 granules/day) possess extra information over the standard AIRS files, e.g., information  
178 on averaging kernel and degree of freedom, including vertical profiles at 100 pressure levels,  
179 against just 28 in the standard product.

180

181 The support product profiles contain 100 levels between 1100 and 0.016 mbar. While it has a  
182 higher vertical resolution, the vertical information content is no greater than the standard product.  
183 The information on averaging kernels and degree of freedoms (DOFs) is utilized to understand the  
184 retrieved products more comprehensively. The DOFs of ozone, a measure of significant eigen  
185 functions used in the AIRS retrieval, has an average value of 1.36 over the tropical latitude band  
186 (Maddy et al., 2008) (Table S1), while over the balloon collocated region an average DOFs of 1.62  
187 is observed (Figure S1). In the present study, best quality retrieval ( $O_3\_QC=0$ ), associated with  
188 cloud fraction less than 80%, and retrievals with degrees of freedom (DOF)  $> 0.04$  are utilized.  
189 However, analysis of cloud fraction over our collocated position shows (Figure S2) that except in  
190 July and August the cloud fraction does not exceed  $\sim 50 \pm 12\%$ , whereas, during July and August  
191 the maximum cloud fraction of about  $\sim 65 \pm 20\%$  is seen.

192

193

194

195

196





197 **2.1.2 IASI (NOAA/CLASS)**

198 The Infrared Atmospheric Sounding Interferometer (IASI) onboard MetOp satellites with a  
199 primary focus on meteorology than climate and atmospheric chemistry monitoring, is a nadir  
200 viewing Michelson interferometer (Clerbaux et al., 2007). The first MetOp satellite was launched  
201 in October 2006 (MetOp-A) and IASI was declared operational in July 2007. MetOp is a polar  
202 sun-synchronous satellite having descending and ascending nodes at 09:30 and 21:30 LT,  
203 respectively. IASI measures in the IR part of the EM spectrum at a horizontal resolution of 12 km  
204 at nadir up to 40km over a swath width of about 2,200 km. IASI covers an infra-red spectral range  
205 between 3.7 to 15.4  $\mu\text{m}$  with a total of 8461 spectral channels, out of which 53 channels around  
206 9.6  $\mu\text{m}$  are utilized for ozone retrieval. IASI level 2 ozone products provided by NOAA National  
207 Environmental Satellite Data and Information Service (NESDIS) Center for Satellite Application  
208 and Research (STAR) are used in this study. The IASI (NOAA/CLASS) ozone product is retrieved  
209 based on the AIRS algorithm and has various quality control flags (Table S2). Only QC=0 data  
210 which represents a successful IR+MW retrieval is used.

211

212 **2.1.3 CrIS/ATMS (NUCAPS)**

213 The Cross-track Infrared Sounder (CrIS) and Advanced Technology Microwave Sounder (ATMS)  
214 sounding system onboard the Suomi NPP satellite were launched in 2011 to feature the high  
215 spectral-resolution (“hyperspectral”) observations of earth’s atmosphere. The CrIS instrument is  
216 an advanced Fourier transform spectrometer with an ascending node 13:30 LT and flies at a mean  
217 altitude of 824 km and performs fourteen orbits per day. It measures high-resolution IR spectra in  
218 the spectral range 650 - 2550  $\text{cm}^{-1}$  with a total of 1305 channels. The ATMS is an MW sounder  
219 with a total of 22 channels ranging from 23 to 183 GHz. These two instruments CrIS and ATMS



220 operate in an overlapping field-of-view (FOV) formation, with ATMS FOVs re-sampled to match  
221 the location and size of the 3×3 CrIS FOVs for retrieval under clear to partly cloudy conditions.  
222 Here the NUCAPS algorithm-based ozone product of CrIS is utilized. The NOAA Unique  
223 CrIS/ATMS Processing System (NUCAPS) is a heritage algorithm developed by the STAR team  
224 based on the AIRS retrieval algorithm (Susskind et al., 2003, 2006). The NOAA implemented  
225 NUCAPS algorithm is a modular architecture that was specifically designed to be compatible with  
226 multiple instruments. The same retrieval algorithms are currently used to process the AIRS/AMSU  
227 suite (operations since 2002), the IASI/AMSU/MHS suite (operationally since 2008), and now the  
228 CrIS/ATMS suite (approved for operations in January 2013). Here again, various quality controls  
229 for retrieved data are provided by the NUCAPS science algorithm team, and we used QC=0  
230 (successful IR+MW retrieval) for lesser discrepancies in our evaluation. These research products  
231 follow a similar retrieval algorithm as developed by the AIRS science team, which gives us further  
232 opportunity to assess the AIRS retrieval algorithm for IASI and CrIS radiances.

233

#### 234 **2.1.4 Ozonesonde**

235 Electrochemical concentration cell (ECC) ozonesondes and GPS-radiosondes have been launched  
236 from the Aryabhata Research Institute of Observational Sciences (ARIES) (29.4° N, 79.5° E, and  
237 1793 m elevation) Nainital (Figure 1), a high-altitude site in central Himalaya, since 2011 (Ojha  
238 et al., 2014; Rawat et al., 2020), the only facility in the Himalayan region having regular flights.  
239 ECC ozonesonde relies on the oxidation reaction of ozone with potassium iodide (KI) solution  
240 (Komhyr et al., 1995) to measure ozone partial pressure in the ambient atmosphere. The typical  
241 vertical resolution of ozonesonde is about 100 – 150 m and has a precision of better than  $\pm$  (3–5)  
242 % with an accuracy of about  $\pm$  (5–10) % up to 30 km altitude under standard operating procedures



243 (Smith et al., 2007). The ozonesonde is connected to iMet-radiosonde via V7 electronic interface  
244 where radiosonde consists of GPS, PTU, and a transmitter to transmit signals to the ground. Due  
245 to higher accuracy and in-situ measurement, ozonesonde has been widely used worldwide for  
246 satellite and model validation (Divakarla et al., 2008; Nassar et al., 2008; Monahan et al., 2008;  
247 Kumar et al., 2012a, 2012b; Dufour et al., 2012; Verstraeten et al., 2013; Rawat et al., 2020). Both  
248 the ascending and descending data were recorded by ozonesonde, however, due to time lag in  
249 descending records only ascending data is utilized (Lal et al., 2013, 2014; Ojha et al., 2014). The  
250 data is collected at the interval of about 10 meters which is averaged over 100 meters interval using  
251 a  $3\sigma$  filter that removes the outlier values (Srivastava et al., 2015; Naja et al., 2016).

252

253 Additionally, collocated and concurrent OMI and Microwave Limb Sounder (MLS) observations  
254 are also used to study the tropospheric ozone, UTLS, and total ozone column due to their  
255 reasonable sensitivity and well-validated retrievals (Veefkind et al., 2006; Zeimke et al., 2006;  
256 Fadnavis et al., 2014; Wang et al., 2021). The best quality data of MLS with data flags, i.e.,  
257 status=even, quality>0.6, and convergence<1.18 is utilized (Barré et al., 2012). A slightly different  
258 collocation criterion of  $3^{\circ}\times 3^{\circ}$  grid box and daytime collocation is utilized for MLS in this work,  
259 due to coarser resolution and to get sufficient matchups.

260

## 261 **2.2 Methods of Analysis**

262 The balloon launch time is mostly around 12:00 IST (Indian Standard Time, which is 5.5 hours  
263 ahead of GMT). The Aqua satellite comes over the Indian region around 1:30 pm and 1:30 am  
264 IST. Hence for collocation, only noontime (ascending) data (or  $\pm 3$  hours of balloon launch) with  
265  $1^{\circ}\times 1^{\circ}$  spatial collocation were chosen in this evaluation. However, for some days, there was no



266 noontime granule in AIRS retrieval (nearly 35 out of total 242 soundings), then we used loose  
267 collocation of  $\pm 1$  day. However, no significant changes were seen after such flexible collocation.  
268 Most of the ozonesondes have burst altitudes near 10hPa, hence AIRS ozone profiles are evaluated  
269 from surface to 10hPa.

270

271 Although suitable collocation criteria have been defined for a fair comparison, still different  
272 vertical resolutions of the two data sets (ozonesonde  $\sim 100$  m and AIRS  $\sim 1-5$  km) make the  
273 meaningful comparison difficult (Smit et al., 2007; Maddy and Barnet 2008). The difference in  
274 vertical resolution and retrieval sensitivity has to be accounted for a meaningful comparison.  
275 Hence, ozonesonde data were first interpolated at all AIRS Radiative Transfer Algorithm (RTA)  
276 layers from surface to burst altitude, then ozonesonde profiles are smoothed according to the AIRS  
277 averaging kernel and a-priori profile (ML climatology), leading to a vertical profile [ozonesonde  
278 (AK)] representing what AIRS would have measured for the same ozonesonde sampled  
279 atmospheric air mass in the absence of any other error affecting satellite observations. According  
280 to Rodgers et al., (2000), the smoothing of the true state can be characterized as follows:

281 
$$X_{\text{est}} = X_0 + A'(X_{\text{sonde}} - X_0) \quad (1)$$

282 The AIRS provides averaging kernels information at 9 pressure levels (Figure 2b) whereas the  
283 AIRS RTA has 100 pressure levels. So following ozone vertices (Table S3) and formulating  
284 trapezoid matrix (Figure 2a, the details regarding the calculation of trapezoid matrices are given  
285 in AIRS/AMSU/HSB Version 6 Level 2 Product Levels, Layers and Trapezoids), we convert 9  
286 levels AIRS averaging kernels to 100 levels averaging kernels using following defined operation.

287 
$$A' = F \times A_{\text{trapezoid}} \times F' \quad (2)$$



288 Where  $A_{trapezoid}$  and  $F$  are averaging kernel matrices and trapezoid matrices ( $F'$  is pseudo-inverse  
289 of  $F$ ).  $A_{trapezoid}$  is a given product while  $F$  is calculated for given ozone vertices (Table S3).

290

291 Further, in the thermal IR spectrum, the contribution of ozone or any other trace gas towards  
292 emission/absorption of IR radiation in the radiative transfer equation depends on the exponent of  
293 layer integrated column amounts (Maddy et al., 2008). Hence logarithmic changes in layer column  
294 density are more linear than absolute changes. So logarithmic equations are used instead of eq. 1  
295 for smoothing ozonesonde data in the present study.

$$296 \quad \ln(X_{est}) = \ln(X_0) + A' \{ \ln(X_{sonde}) - \ln(X_0) \} \quad (3)$$

297 Where  $X_{est}$ ,  $X_{sonde}$ , and  $X_0$  are smooth ozonesonde or ozonesonde (AK), true ozonesonde, and first  
298 guess (ML climatology) profiles, respectively.

299 More details on the calculation of averaging kernels can be found in AIRS documents  
300 (AIRS/AMSU/HSB Version 6 Level 2 Product Levels, Layers and Trapezoids) or in available  
301 literature (Maddy and Barnet 2008; Irion et al., 2008). A typical averaging kernels matrix and other  
302 parameters are shown in Figure 2. Here Figure 2a shows a typical trapezoid matrix, Figure 2b  
303 shows the averaging kernels at 9 pressure levels, Figure 2c shows constructed averaging kernels  
304 at 100 RTA layers, and Figure 2d shows an example for the different ozone profiles convolved  
305 with AKs on 15 June 2011 over the observation site.

306

307

308



### 309 2.3 Statistical Analysis

310 The error analysis for AIRS retrieval with interpolated and smoothed ozonesonde is based on Nalli  
311 et al. (2013, 2018). Bias, root mean squared error (RMSE), and standard deviation (STD) are  
312 studied at various RTA vertical levels from the surface to 10hPa over the Himalayan region. The  
313 finer spatio-temporal collocation utilized here has further minimized the uncertainty and error in  
314 the evaluation. Since the observation site (29.4° N, 79.5° E) is at a latitude lower than 45°; hence  
315 there is a lesser overlap of satellite passes, and mostly a few nadir scans are close to the observation  
316 site (mostly daytime granules in range of 75 to 85). Hence all the daytime observations of AIRS  
317 are close to ± 3 hours of temporal collocation to the ozonesonde launch and possess a lesser chance  
318 of time mismatch.

319

320 Given the collocated ozone mixing ratio profiles for satellite, ozonesonde (AK) and in situ truth  
321 (ozonesonde) observations, the statistical errors are calculated as follows

322

$$323 \quad \text{RMSE}(\Delta O_l) = \sqrt{\frac{\sum_{j=1}^{j=n} W_{l,j} \times (\Delta O_{l,j})^2}{\sum_{j=1}^{j=n} W_{l,j}}} \quad (4)$$

324

$$325 \quad \text{Bias}(\Delta O_l) = \frac{\sum_{j=1}^{j=n} W_{l,j} \times (\Delta O_{l,j})}{\sum_{j=1}^{j=n} W_{l,j}} \quad (5)$$

326 Here  $l$  runs over different RTA layers and  $j$  runs for all collocated profiles,  $\Delta O_{l,j}$  the fractional  
327 deviation is taken to be the absolute deviation divided by the observed value.

328  $\Delta O_{l,j} = \left( \frac{O_{l,j}^R - O_{l,j}^T}{O_{l,j}^T} \right)$ , where  $O^T$  and  $O^R$  are ozonesonde/ozonesonde (AK) and satellite retrieved

329 ozone mixing ratio respectively.



330  $W_{i,j}$  is the weighting factor and assumes one of three forms  $W_0 = 1$ ,  $W_1 = O^R$  and  $W_2 = (O^R)^2$  and  
 331 for ozone to minimize skewing impact due to large variation in mixing ratio at different altitudes,  
 332 we have used the  $W_2$  weight factor as suggested by other sounder science team (Nalli et al., 2013,  
 333 2018).

334 The Standard deviation (STD) is then calculated as follows

335

$$336 \quad \text{STD}(\Delta O_i) = \sqrt{[RMSE(\Delta O_i)]^2 - [Bias(\Delta O_i)]^2} \quad (6)$$

337

338 Further to check the strength of the linear relationship between the satellites retrieved data and  
 339 ozonesonde data the square of Pearson's correlation coefficient is also calculated as follows

$$340 \quad r = \left[ \frac{\sum_{j=0}^{j=n} (o_j^T - o^T \text{avg})(o_j^R - o^R \text{avg})}{\sqrt{\sum_{j=0}^{j=n} (o_j^T - o^T \text{avg})^2 \sum_{j=0}^{j=n} (o_j^R - o^R \text{avg})^2}} \right] \quad (7)$$

341

342 Where the summation is over different pairs of satellite-ozonesonde matchup values.

343

#### 344 **2.4 Estimation of Columnar Ozone**

345 The total column ozone (TCO) from ozonesonde is calculated by integrating the ozone mixing  
 346 ratio from the surface to burst altitude and then adding residual ozone above burst altitude. Here  
 347 the residual ozone is obtained from satellite-derived balloon-burst climatology (BBC) (Peters et  
 348 al., 1997). The discrete integration for calculation of total ozone column (DU) between defined  
 349 boundaries is performed as follows:

$$350 \quad \text{Total column ozone} = 10^7 \times \left(\frac{RT_o}{g_o P_o}\right) \times \sum_{j=1}^{j=n} 0.5 \times (VMR[i] + VMR[i + 1]) \times (P[i] - P[i + 1]) \quad (8)$$

351



352 Where  $P$  is ambient pressure in hPa, VMR volume mixing ratio of ozone in ppbv,  $R$  ( $= 287.3 \text{ JKg}^{-1}$   
353  $\text{K}^{-1}$ ) gas constant,  $g_0$  ( $= 9.88 \text{ ms}^{-2}$ ),  $P_0$  ( $= 1.01325 \times 10^5 \text{ Pa}$ ) and  $T_0$  ( $= 273.1 \text{ K}$ ) standard  
354 temperature.

355 The UTLS ozone column (DU) is also calculated using Eq. (8), where the UTLS region is defined  
356 between 400 hPa to 70 hPa (Bian et al., 2007). Additionally, the tropospheric ozone column (DU)  
357 is calculated for ozonesonde utilizing the Eq. (8) with boundaries from the surface to the  
358 tropopause. The tropopause height from balloon-borne observations is estimated using the lapse  
359 rate method as well as the AIRS-derived tropopause is used and shown in Figure 3. However for  
360 OMI and MLS tropospheric ozone residual method is used which calculates the tropospheric ozone  
361 column by subtracting the OMI total column from MLS stratospheric ozone column.

362

### 363 **3. Results and Discussion**

#### 364 **3.1 Spatial Distribution: Ozonesonde and AIRS**

365 The spatial distributions of ozone obtained using all ozone sounding data during four seasons are  
366 shown in Figure 4 and spatial distributions in AIRS retrieved ozone is also shown for the  
367 comparison. To obtain the AIRS ozone, the nearest swath of AIRS ozone observations is  
368 interpolated to the balloon locations and altitude. Altitude variations of the balloon along longitude  
369 is shown in Figure S3. The balloon drifts to a very long distance during winter followed by autumn  
370 and spring. During these seasons, balloon reaches to Nepal also. The wind reversal takes place  
371 during the summer-monsoon when the balloon drifted towards IGP regions (Figure 4). The spatial  
372 distributions in ozone from AIRS are more or less similar to the distributions those from  
373 ozonesonde. The bias and coefficient of determination ( $r^2$ ) between ozonesonde and AIRS ozone  
374 is studied along the longitude and latitude (Figures S3 and S4). Lower biases (lesser than 10%)





375 and higher  $r^2$  are seen in the lower and middle troposphere and notable biases in the upper  
376 troposphere and lower stratosphere regions. The poor correlation ( $<0.4$ ) and larger biases of up to  
377 28% are seen at certain longitudes those are associated with higher altitudes ( $> 20$  km). Around  
378 the balloon launch site (Nainital, 79.45 E) highest  $r^2$  score of 0.98 and low bias of 1.4% is observed,  
379 which remain higher ( $r^2$ ) and lower (bias) up to 80° E (Figure S3).

380

### 381 **3.2 Ozone Soundings and AIRS Ozone Profiles**

382 Figure 5 shows the average monthly ozone profiles for different collocated data sets (ozonesonde,  
383 ozonesonde (AK), AIRS, and AIRS apriori) during seven-year periods from the surface to 10 hPa  
384 altitude. The percentage difference between ozonesonde and AIRS ozone values at 706, 617, 496,  
385 103, 29, and 14 hPa altitudes are mentioned and the zoomed variations in the lower tropospheric  
386 ozone (surface to 200 hPa) are also shown in the insets. AIRS slightly ( $\sim 10\%$ ) underestimate ozone  
387 in the lower troposphere during most of the months, except the summer-monsoon (June-August),  
388 where an overestimation of up to 20% is observed. In the middle troposphere, around 300 hPa, an  
389 underestimation in the range 1 - 17% is seen for all months with an approaching tendency of  
390 ozonesonde (AK) towards the true ozonesonde profiles. However, near the tropopause region,  
391 AIRS retrievals considerably overestimate ozone by up to 102%. The overestimation was the  
392 highest for the winter season (82 - 102%), followed by the spring, autumn, and the lowest for the  
393 summer-monsoon season (10 - 27%). In the stratosphere, where the sensitivity of AIRS is higher  
394 (Figure 2c), the ozonesonde and AIRS differences were relatively lower with an underestimation  
395 in between 5 - 21%.

396



397 As expected, the difference between ozonesonde and AIRS is significantly reduced (Table 1) after  
398 applying the averaging kernel or accounting for the sensitivity difference. This reduction was more  
399 notable for the summer monsoon period near the tropopause, where the difference reduced from  
400 92% to 19%, providing improvement by 72%. The improvement is as high as 100% on monthly  
401 basis. Additionally, relative difference profiles were also analyzed for individual soundings as well  
402 for the different seasons (Figure S5). Higher differences of about 150% between AIRS and  
403 ozonesonde ozone observations were seen in the upper troposphere and lower stratospheric  
404 (UTLS) region. The higher difference during winter and spring between these observations in the  
405 UTLS region could be due to recurring ozone transport via tropopause folding over the observation  
406 site. Such events may remain undetected by AIRS due to lower vertical resolution leading to  
407 missing of some tropopause folding events at lower altitudes (Figure 3). However, in the lower  
408 troposphere, larger differences between ozonesonde and AIRS during summer-monsoon are seen,  
409 which are due to low ozone and cloudy conditions. The arrival of cleaner oceanic air during south-  
410 west monsoon brings ozone poor air and frequent cloudy conditions over the northern India that  
411 weakens the photochemical ozone production (Naja et al., 2014; Sarangi et al., 2014).

412

413 Figure 6 shows the yearly time series analysis of average ozone mixing ratio at three defined layers,  
414 characterizing the middle troposphere (600 - 300 hPa), the upper troposphere (300 - 100 hPa), and  
415 lower/middle stratosphere (100 - 10 hPa), respectively. A prominent seasonality was seen in the  
416 time series throughout the years, which is quite clear in the upper troposphere (300 - 100 hPa).  
417 The ozone seasonality contrast reflects the influence of summer-monsoon and winter seasons.  
418 Total column water vapor and monsoon index is also shown in Figure 6 and both show a tendency  
419 of anti-correlation with ozone in 300 - 100 hPa region. The monsoon index is estimated (Wang et



420 al., 2001) by the difference between zonal (U) wind at 850hPa over the Arabian Sea (40E-80E,  
421 5N-15N) and over the central Indian landmass (70E-90E, 20N-30N). The anti-correlation with  
422 total column water vapor is slightly higher for AIRS ozone (~0.26) and it is somewhat lower with  
423 ozonesonde (~0.15) in 300-100 hPa region. The relative difference of AIRS ozone with  
424 ozonesonde and ozonesonde(AK) in the upper tropospheric region also shows an anti-correlation  
425 (Figure S6) of 0.17 and 0.55 with total column water vapor and of 0.27 and 0.76 with monsoon  
426 index, respectively.

427

428 In general, the positive values of the monsoon index correspond to strong monsoon, and negative  
429 values correspond to weak monsoon periods (Wang et al., 2001). During the weak monsoon, there  
430 is relatively drier air, lower cloud cover, and higher surface temperature, leading to a larger net  
431 ozone production and relatively low upward redistributions compared to the strong monsoon  
432 period. Thereby anti-correlation between ozone and monsoon index. The drier or low water vapor  
433 seasons (or negative MI) show larger ozone differences between AIRS and ozonesonde, which  
434 may be arising due to the influence of ozone-sensitive water vapor (WV) channels in mid-Infra-  
435 red regions. Further, in the middle troposphere (600-300 hPa), a secondary ozone peak in post-  
436 monsoon is observed, arising from the higher ozone mixing ratio after biomass burning events  
437 over northern India (Bhardwaj et al., 2015) that seems to be missing in the AIRS ozone.

438

439 In the middle troposphere (600 - 300 hPa), AIRS retrievals show differences of more-or-less  
440 similar magnitude with respect to both ozonesonde and ozonesonde (AK) (Figure S6). However,  
441 in the lower/middle stratosphere (100 - 10 hPa), a considerable reduction of difference is seen after  
442 applying the averaging kernel to ozonesonde (blue line in figure S6), which shows the need to



443 account for the sensitivity of AIRS in the evaluation. Further, a systematic increase of standard  
444 deviation is also seen with the altitude. The higher standard deviations in the upper tropospheric  
445 and stratospheric regions are mainly due to higher ozone variability associated with stratosphere-  
446 troposphere exchange (STE) processes over the Himalayan region (Naja et al., 2016; Bhardwaj et  
447 al., 2018).

448

### 449 **3.3 Statistical Analysis of AIRS Ozone Profiles**

450 Error analysis of AIRS retrieved ozone over the Himalayan region is performed with spatio-  
451 temporal collocated ozonesonde observations as a reference. The methodology to calculate the  
452 root mean square error (RMSE), bias, and standard deviation (STD) is described in section 2.3.  
453 W2 weighting statistics is utilized due to abrupt changes of atmospheric ozone with altitude. Here  
454 bias, RMSE, and STD between AIRS and ozonesonde are calculated at different RTA layers from  
455 surface to 10 hPa. Figure 7 shows the average variation of bias, RMSE, and STD at different RTA  
456 layers from surface to 10 hPa over this region. In general, higher positive bias (~65%), RMSE  
457 (~65%), and STD (~25%) in AIRS ozone is seen in the UTLS region. In the lower and middle  
458 troposphere, the AIRS ozone retrieval is negatively biased (0 - 25%), which increases gradually  
459 from the surface to higher altitudes (~ 350hPa). A negative bias was also seen in the stratosphere  
460 of about 15%. Similar to the bias, the RMSE and STD are smaller in the lower troposphere and  
461 stratosphere with values of nearly 15% and 10%, respectively. The higher statistical errors in the  
462 upper troposphere and the lower stratospheric region could be due to lower ozone partial pressure  
463 and frequent stratospheric to tropospheric transport events over the Himalayas (Rawat et al., 2020),  
464 which introduces error either after mismatch of events in AIRS coarser vertical resolution or due  
465 to complex topography. Additionally, the AIRS tropopause frequency distribution shows less



466 ability of AIRS to capture deep intrusion events (Figure 3). Further, AIRS trace gas retrieval  
467 largely depends on successful temperature retrieval and uses temperature retrieval as an input  
468 parameter (Maddy et al., 2008). Hence, temperature retrieval error could also propagate to ozone,  
469 and statistical error analysis of AIRS temperature shows relatively higher biases (~ 2 K) in the  
470 upper tropospheric region (Figure S7).

471

472 The statistical error analysis was more or less similar for both true and smoothed ozonesonde  
473 profiles. However, notable reduction and vertical shifts were also observed after applying the  
474 averaging kernel matrix to the true ozonesonde throughout the profile. A shift of the error peak is  
475 seen from the lower stratosphere to the upper troposphere. This could be due to the higher  
476 sensitivity of AIRS retrieval in the lower stratosphere, which would have minimized the error at  
477 these particular altitudes. However, in the upper troposphere, higher contribution of a-priories as  
478 well as other factors (i.e., STE) might have resulted in larger biases and errors.

479

480 The histogram remainder between AIRS and ozonesonde is also studied at various defined layers  
481 (Figure 8). AIRS mostly underestimates ozone with a mean bias of 2.37 ppbv, 9.29 ppbv, and  
482 459.8 ppbv in 800 - 600 hPa, 600 - 300 hPa, and 100 - 10 hPa layers, respectively, while in the  
483 upper troposphere (300 - 100 hPa) AIRS overestimated with a mean bias of 43.22 ppbv.  
484 Furthermore, remainder distributions are skewed towards the negative values in the lower  
485 stratosphere and towards positive values in the upper troposphere. More symmetric distribution  
486 over the negative axis is observed in the middle and lower troposphere. We also studied the  
487 correlation profiles for different seasons (Figure 8 right panel). A strong correlation is seen in the  
488 lower and middle troposphere for spring and summer, while a poor correlation for winter and



489 autumn. The correlation between AIRS and ozonesonde (AK) shows a higher value in the lower  
490 stratosphere (0.98), followed by in the upper troposphere (0.81), the middle troposphere (0.52),  
491 and lower troposphere (0.52).

492

### 493 **3.4 Assessment of AIRS Retrieval Algorithm with IASI and CrIS Radiance**

494 The MetOp/IASI and Soumi-NPP/CrIS radiance-based ozone products are assessed using  
495 ozonesonde data over the central Himalayan region for one year (April 2014 to April 2015),  
496 utilizing a total of 32 soundings. Here, the IASI and CrIS based ozone retrievals are research  
497 products provided by NOAA, whose retrieval is based on the AIRS retrieval algorithm. For IASI,  
498 due to the 09:30 ascending nodes (morning overpass in India),  $\pm 6$  h loose temporal collocation is  
499 used. However, CrIS and AIRS follow the same collocation due to a similar noontime overpass.  
500 The IASI, CrIS, and AIRS sensors have 8461, 1305, and 2378 IR channels respectively. Hence,  
501 analyzing their satellite ozone products further helps to assess the AIRS retrieval algorithm for  
502 different IR radiances and channel sets.

503

504 Figure 9a shows the seasonal ozone profiles obtained from three IR satellite sensors along with  
505 ozonesonde for one year period. All sensors successfully captured the ozone altitude gradient and  
506 the ozone peak height. Higher ozone concentrations during spring throughout the troposphere are  
507 captured well by all satellite sensors. Higher ozone during spring and winter in the UTLS region  
508 are observed by AIRS and IASI similar to ozonesonde but not by CrIS. At the same time, CrIS  
509 sensitivity looks relatively low, where the possible role of the number of channels can be seen.  
510 However, IASI and AIRS have effectively captured the ozone seasonal variability.

511



512 Figure 9b shows the weighted statistical error analysis of IASI, CrIS, and AIRS ozone retrieval  
513 with the true ozonesonde observations. Here, the difference in sensitivity of the two data sets is  
514 not accounted for as this section's primary aim is to assess the AIRS retrieved algorithm using  
515 different IR sensor radiances and channel sets. All three space-borne sensors overestimated UTLS  
516 ozone by more than 50%, however, in the stratosphere and lower troposphere, the bias was slightly  
517 lower and it is somewhat underestimated. Similar to bias, the RMSE and STD were also higher in  
518 the UTLS region by more than 80% and 60%, respectively. A consistent larger error in the UTLS  
519 region for three IR satellite sensors that share the same radiative transfer model and retrieval  
520 algorithm shows the possible influence of complex topography and the various STE processes in  
521 introducing errors in retrieval processes, apart from input a-priories of the retrieval.

522

523 Additionally, Pearson correlations between ozonesonde and IASI, CrIS, and AIRS are also studied  
524 at four atmospheric layers (i.e., 600-800 hPa, 300-600 hPa, 100-300 hPa, and 10-100 hPa) (Table  
525 2). A relatively stronger positive correlation is found in the stratosphere (10-100 hPa), which was  
526 highest for CrIS followed by AIRS and IASI (98%, 97%, and 91%, respectively), and a relatively  
527 low correlation is observed in the middle troposphere (300-600 hPa) for AIRS and IASI (~ 44%  
528 and 31%), while CrIS shows the poor correlation in the lower troposphere about 9%.

529

### 530 **3.5 Columnar Ozone**

#### 531 **3.5.1 Total Column Ozone (TCO)**

532 Figure 10a shows the variations in monthly average total column ozone (TCO) from ozonesonde,  
533 AIRS, and OMI during 2011 - 2017. In general, the TCO is higher during spring, which  
534 subsequently drops in summer-monsoon. AIRS TCO shows a bimodal monthly variation which is



535 not seen in the ozonesonde and OMI observations, otherwise its monthly variation is in reasonable  
536 agreement with ozonesonde. The OMI TCO are in good match with the ozonesonde with a  
537 maximum difference of up to about 5 DU. Table 3 shows the difference in the TCO between  
538 AIRS, OMI, and ozonesonde. AIRS shows considerable overestimation in the range of 0.2 - 22  
539 DU for some months while notable underestimation (1.8 – 10.7 DU) for others, with respect to  
540 both ozonesonde and OMI. The correlation between AIRS TCO and ozonesonde TCO is found to  
541 be lower (about 0.5), which has improved significantly (0.65) after applying the averaging kernel  
542 (Table S4). To further understand the cause of bimodal variations in AIRS (higher ozone during  
543 August, September, and October), the AIRS ozone profiles were integrated between various  
544 altitude ranges along with corresponding ozonesonde columns, and we found the elevated total  
545 ozone during post-monsoon is mainly contributed from the altitude above 50 hPa.

546

### 547 **3.5.2 UTLS Ozone Column**

548 Figure 10b shows the variations in monthly average UTLS ozone column for collocated and  
549 concurrent observations of AIRS, MLS, and ozonesonde during 2011 - 2017. The UTLS region  
550 extends between 400 hPa to 70 hPa (Bian et al., 2007). In contrast to TCO, a higher ozone in UTLS  
551 is seen during the winter and spring (~ 45 DU) when there are recurring downward transport  
552 events, while a clear drop of the column during the summer-monsoon shows the convective  
553 transport of cleaner oceanic air to the higher altitudes. All the collocated observations are able to  
554 capture the monthly variation effectively; however, there is a substantial overestimation by more  
555 than 7 DU (Table S5) during winter and spring for both AIRS and MLS. Further, the higher  
556 standard deviations during winter and spring show the larger variations of the ozone in the UTLS  
557 region. Though there were notable overestimations compared to ozonesonde, still UTLS monthly





558 variations are captured well by AIRS with a correlation of up to 90% (Table S4). Such biases in  
559 satellite retrieval arise due to input parameters that can be improved by using more accurate initial  
560 parameters and surface emissivity.

561

### 562 **3.5.3 Tropospheric Ozone Column**

563 Figure 10c shows the variations in monthly average tropospheric ozone column utilizing various  
564 collocated data sets during 2011 - 2017. The tropospheric ozone column is calculated by  
565 integrating ozone profiles from the surface to the tropopause. WMO-defined lapse rate calculation  
566 method is used to calculate tropopause height from balloon-borne and AIRS observations (Figure  
567 3). Higher tropospheric ozone is observed during the spring and early summer ( $> 45$  DU) when  
568 annual crop-residue burning events occur over northern India, apart from downward transport from  
569 the stratosphere. Few cases of downward transport are discussed in the next section. The  
570 tropospheric ozone column drops rapidly during the summer-monsoon when pristine marine air  
571 reaches Nainital. A slight increase of column is also seen during the autumn, which is again  
572 influenced by post-monsoon crop residue burning practices in northern India (Bhardwaj et al.,  
573 2016). The AIRS is able to capture the monthly variations very effectively; however, there are  
574 larger biases. The biases with ozonesonde are higher when the tropopause is taken from the  
575 balloon-borne observation, while with AIRS provides tropopause, the biases are lesser or mostly  
576 within the one sigma limit. Like AIRS, the OMI/MLS column is in good agreement and able to  
577 produce monthly variations; however, there are larger differences during winter and spring of more  
578 than 10 DU. The tropospheric ozone column from ozonesonde is different for balloon-borne LRT  
579 and AIRS tropopause, whose possible reason could be due to the lower vertical resolution of AIRS,  
580 which will calculate tropopause with an uncertainty of 1-2 km (Divakarla et al., 2006), and on



581 average a lower tropopause pressure (or higher altitude) by 28% is calculated by AIRS compare  
582 to ozonesonde measurements (Figure 3).

583

### 584 **3.6 Case Studies of Biomass Burning and Downward Transport**

585 Over the northern India, extensive agriculture practices and forest fires influence ozone at the  
586 surface and higher altitudes (Kumar et al., 2011; Bhardwaj et al., 2016; Bhardwaj et al., 2018).

587 Based on MODIS fire counts, the days in between 1 March to 15 April over northern India are  
588 classified as the low fire periods (LFP) as considered in previous studies over this region. The high

589 fire period (HFP) is classified when the fire counts over the observational site are more than the  
590 median fire counts in the biomass burning period, typically from mid-April to mid-June (Bhardwaj  
591 et al., 2016). A total of 32 and 33 collocated soundings are classified as HFP and LFP, respectively.

592 Figure 11 (left) shows the average ozone profiles up to 6 km from ozonesonde and AIRS  
593 observations during HFP and LFP. The ozonesonde data show enhancement in ozone by about 5  
594 ppbv to about 11 ppbv during HFP as compared to LFP that is accounting to 5-20% increase. It is  
595 important to mention that enhancement is greater at higher altitude region. The enhancement is  
596 slightly lower (10-15%) in AIRS profile, where most of it is contributed by the a priori profile  
597 (Figure S8).

598

599 Deep stratospheric intrusion or the downward transport (DT) of ozone-rich air from the  
600 stratosphere to the troposphere significantly influences ozone profiles over the subtropical regions  
601 (Collins, et al., 2003; Zhu, et al., 2006). Over the subtropical Himalayas, such ozone intrusions are  
602 observed during the winter and the spring seasons (Zhu et al., 2006; Ojha et al., 2014). A total of  
603 10 collocated soundings are classified as DT events for ozonesonde and AIRS. Figure 11 (right)



604 shows ozone profiles from ozonesonde (AK) and AIRS observations for high ozone DT events as  
605 well as the average ozone profiles of corresponding months excluding the DT event. Though there  
606 are persistent positive biases in AIRS ozone profile compared to ozonesonde in the middle/upper  
607 troposphere, still both the observations have captured the influence of the downward transport on  
608 the ozone profile very effectively and show an increase in ozone of 10 - 20% in altitude range 2 -  
609 16 km. Ozonesonde based observations have shown about two fold increase in upper-middle  
610 tropospheric ozone due to downward ozone transport over this region (Ojha et al., 2014). Further,  
611 the first guess profile's contribution to AIRS retrieval during DTs is negligible (Figure S8) and  
612 shows main contribution from the observations itself. So despite the persistent biases in the AIRS  
613 and ozonesonde observations, AIRS is able to capture the influences of downward transport (DT)  
614 on ozone profile notably well.

615

### 616 **3.7 Ozone Radiative Forcing**

617 Radiative forcing is a valuable metric to estimate the radiative impacts of any anthropogenic or  
618 natural activity on the climate system (Ramaswamy et al., 2001). It measures the net radiation at  
619 the surface, tropopause, and the top of the atmosphere due to any atmospheric constituents. Here  
620 we discuss the ozone radiative forcing (RF) at the surface in the ultraviolet (UV) spectral range  
621 (Antón et al., 2013; Mateos et al., 2020) using the ozonesonde, OMI, and AIRS total column ozone  
622 (TCO) data. The RF is calculated based on Antón et al. (2014), relative to 1979 utilizing TOMS  
623 TOC data in 1979, monthly averaged solar zenith angles of site, clearness index based on  
624 Chakraborty et al., (2014) and Hawas et al., (1984), and respective monthly average TCO data of  
625 AIRS, OMI, and ozonesonde. Rather than quantifying the RF values here, our primary focus is to  
626 show how the discrepancies of satellite ozone data (mainly AIRS) can impact the calculation of



627 RF values. Figure 12 shows the seasonal average ozone radiative forcing (RF) relative to 1979.  
628 The annual average ozone RF during 2011 -2017 is 4.86, 4.04, and 2.96 mW/m<sup>2</sup> for ozonesonde,  
629 OMI, and AIRS, respectively. The RF values for ozonesonde and OMI are comparable to Mateos  
630 et al. (2020) (4 mW/m<sup>2</sup>) for the extratropical region. However, for AIRS, the RF value is lower  
631 by 45%. Further, the seasonal average ozone RF (2011-2017) is consistent between ozonesonde  
632 and OMI, while notable differences are seen in AIRS except during the winter season when  
633 differences are marginal (Figure 12). Also from Table 3, it is clear that the higher total ozone bias  
634 during autumn (as high as 22 DU) contributes to higher RF differences in autumn (Figure 12).

635

#### 636 **4. Summary and Conclusions**

637 This study utilized 242 ozone soundings (during 2011 - 2017) conducted over the Himalayan  
638 station (Nainital) to evaluate the AIRS version 6 ozone product and study the performance during  
639 biomass burning events, ozone downward transport events and estimation of ozone radiative  
640 forcing. AIRS ozone retrieval is evaluated in terms of retrieval sensitivity, retrieval biases, retrieval  
641 errors, and ability to retrieve the natural variability of columnar ozone at different altitude regions.  
642 This study is first of its kind in the Himalayan region. The AIRS averaging kernels information  
643 was applied to ozonesonde for a like-for-like comparison to overcome their sensitivity differences.  
644 The monthly profile evaluation shows ozone peak and ozone altitude dependency is captured well  
645 by AIRS retrieval with smaller but notable underestimation (5 - 20%) in the lower-middle  
646 troposphere and stratosphere, while overestimation in the UTLS region as high as 102%. We show  
647 the larger sensitivity of AIRS ozone for the summer monsoon in the UTLS region, where the biases  
648 between AIRS and ozonesonde improved remarkably after applying AIRS averaging kernel  
649 information.



650 The weighted statistical error analysis of AIRS retrieved ozone profiles shows higher positive  
651 biases (65%), RMSE (65%), and STD (25%) in the upper troposphere. In the lower and middle  
652 troposphere, AIRS ozone was negatively biased, apart from the stratosphere. In addition, though  
653 the biases and errors are higher in the upper troposphere, there is a larger correlation of about 81%  
654 showing the capability of AIRS to retrieve upper tropospheric ozone variability with certain  
655 positive biases that can be eliminated by choosing better emissivity inputs or other retrieval inputs.  
656 The AIRS ozone retrieval algorithm was further evaluated using the radiance of IASI and CrIS  
657 sensors; these sensors provided similar error statistics as seen for AIRS.

658

659 The AIRS-derived columnar ozone amounts (i.e., total, UTLS, and tropospheric ozone) are also  
660 evaluated to see whether the ozone variability at different altitude regions is being retrieved  
661 correctly. The UTLS and tropospheric ozone monthly variations are captured well by AIRS with  
662 certain positive biases. However, the total ozone column shows bimodal monthly variations, which  
663 was not evident in the ozonesonde and OMI total ozone observations. Further, we show the higher  
664 total column in AIRS during autumn, which is mostly coming from the stratospheric region above  
665 50 hPa. The capabilities of AIRS to capture various biomass burning and downward transport  
666 events have also been studied. AIRS captures all such events reasonably well with notable  
667 contributions of the first guess, particularly in the biomass burning events.

668

669 Unlike the well-mixed greenhouse gases, the ozone radiative forcing (RF) remains uncertain due  
670 to inadequate budget estimates and complex chemical processes. The total ozone discrepancies of  
671 AIRS lead to show lower RF (by about 45%) and greater uncertainty in this Himalayan region.  
672 Stevenson et al. (2013) have shown that a few percent uncertainties in ozone concentrations can



673 produce a spread of ~17% in ozone RF estimations. Here, the role of in-situ observations from  
674 ozone soundings is shown to be important in improving the satellite retrieved ozone over the  
675 Himalayan region by assessing and providing insights upon its error and bias. This information  
676 could be applied for the ozone product from other satellite data set, having long-term coverage.  
677 This will help in better understanding regional ozone and radiation budgets over this Himalayan  
678 region having complex topography.

679

#### 680 **Acknowledgments**

681 This work is supported by the ISRO-ATCTM project. Help from Deepak and Nitin in balloon  
682 launches and coordination with the air traffic control is highly acknowledged. We are grateful to  
683 Director ARIES for supporting this work. The National Center for Atmospheric Research is  
684 sponsored by the National Science Foundation. SL is grateful to INSA, New Delhi for the position  
685 and Director PRL, Ahmedabad for the support. We highly acknowledge NOAA and NASA-  
686 EARTHDATA online data portals for providing IASI, AIRS, and CrIs label2 data. We would also  
687 like to acknowledge the use of the MODIS fire data through FIRMS archive download. Use of  
688 map from Google earth is also acknowledged.

689

690

691

692 **Data availability:** Satellite data are available in the respective web portal. Ozone sonde data could  
693 be made available on a reasonable request by writing to the corresponding author.

694

695



696 **References**

697 Antón, M., D. Mateos, R. Román, A. Valenzuela, L. Alados-Arboledas, and F. J. Olmo.: A method  
698 to determine the ozone radiative forcing in the ultra-violet range from experimental data, J.  
699 Geophys. Res. Atmos., 119, 1860–1873, doi:10.1002/2013JD020444, 2014.

700

701 Bai, W., Wu, C., Li, J. and Wang, W.: Impact of terrain altitude and cloud height on ozone remote  
702 sensing from satellite, Journal of Atmospheric and Oceanic Technology, 31(4), pp.903-912, 2014.

703

704 Barre, J., Peuch, V.H., Attié, J.L., Amraoui, L.E., Lahoz, W.A., Josse, B., Claeysman, M. and  
705 Nedelec, P.: Stratosphere-troposphere ozone exchange from high resolution MLS ozone analyses,  
706 Atmos. Chem. Phys., 12(14), pp.6129-6144, 2012.

707

708 Bhardwaj, P., Naja, M., Kumar, R. and Chandola, H.C.: Seasonal, interannual, and long-term  
709 variabilities in biomass burning activity over South Asia, Environmental Science and Pollution  
710 Research, 23(5), pp.4397-4410, 2016.

711

712 Bhardwaj, P., Naja, M., Rupakheti, M., Lupascu, A., Mues, A., Panday, A. K., Kumar, R., Mahata,  
713 K. S., Lal, S., Chandola, H. C., and Lawrence, M. G.: Variations in surface ozone and carbon  
714 monoxide in the Kathmandu Valley and surrounding broader regions during SusKat-ABC field  
715 campaign: role of local and regional sources, Atmos. Chem. Phys., 18, 11949–11971,  
716 <https://doi.org/10.5194/acp-18-11949-2018>, 2018.

717



718 Bhartia, P.K., McPeters, R.D., Mateer, C.L., Flynn, L.E. and Wellemeyer, C.: Algorithm for the  
719 estimation of vertical ozone profiles from the backscattered ultraviolet technique, *J. Geophys. Res.*  
720 *Atmos.*, 101(D13), pp.18793-18806, 1996.

721

722 Bian, J., Gettelman, A., Chen, H. and Pan, L.L.: Validation of satellite ozone profile retrievals  
723 using Beijing ozonesonde data, *J. Geophys. Res. Atmos.*, 112(D6), 2007.

724

725 Boynard, A., Hurtmans, D., Koukouli, M.E., Goutail, F., Bureau, J., Safieddine, S., Lerot, C.,  
726 Hadji-Lazaro, J., Wespes, C., Pommereau, J.P. and Pazmino, A.: Seven years of IASI ozone  
727 retrievals from FORLI: validation with independent total column and vertical profile  
728 measurements, *Atmos. Meas. Tech.*, 9(9), pp.4327-4353, 2016.

729

730 Clerbaux, C., Hadji-Lazaro, J., Turquety, S., George, M., Coheur, P.F., Hurtmans, D., Wespes, C.,  
731 Herbin, H., Blumstein, D., Tourniers, B. and Phulpin, T.: The IASI/MetOp1 Mission: First  
732 observations and highlights of its potential contribution to GMES2, *Space Research Today*, 168,  
733 pp.19-24, 2007.

734

735 Coheur, P.F., Barret, B., Turquety, S., Hurtmans, D., Hadji-Lazaro, J. and Clerbaux, C.: Retrieval  
736 and characterization of ozone vertical profiles from a thermal infrared nadir sounder, *J. Geophys.*  
737 *Res. Atmos.*, 110(D24), 2005.

738





739 Collins, W. J., R. G. Derwent, B. Garnier, C. E. Johnson, M. G. Sanderson, and D. S. Stevenson.:  
740 Effect of stratosphere-troposphere exchange on the future tropospheric ozone trend, *J. Geophys.*  
741 *Res.*, 108(D12), 8528, doi:10.1029/2002JD002617, 2003.

742

743 Cristofanelli, P., Putero, D., Adhikary, B., Landi, T.C., Marinoni, A., Duchi, R., Calzolari, F., Laj,  
744 P., Stocchi, P., Verza, G. and Vuillermoz, E.: Transport of short-lived climate forcers/pollutants  
745 (SLCF/P) to the Himalayas during the South Asian summer monsoon onset, *Environmental*  
746 *Research Letters*, 9(8), p.084005, 2014.

747

748 Divakarla, M., Barnet, C., Goldberg, M., Maddy, E., Wolf, W., Flynn, L., Xiong, X., Wei, J., Zhou,  
749 L. and Liu, X.: Validation of Atmospheric Infrared Sounder (AIRS) temperature, water vapor, and  
750 ozone retrievals with matched radiosonde and ozonesonde measurements and forecasts, In  
751 *Multispectral, Hyperspectral, and Ultraspectral Remote Sensing Technology, Techniques, and*  
752 *Applications*, International Society for Optics and Photonics, Vol. 6405, p. 640503, 2006.

753

754 Divakarla, M., Barnet, C., Goldberg, M., Maddy, E., Irion, F., Newchurch, M., Liu, X., Wolf, W.,  
755 Flynn, L., Labow, G. and Xiong, X.: Evaluation of Atmospheric Infrared Sounder ozone profiles  
756 and total ozone retrievals with matched ozonesonde measurements, ECMWF ozone data, and  
757 Ozone Monitoring Instrument retrievals, *J. Geophys. Res. Atmos.*, 113(D15), 2008.

758

759 Dufour, G., Eremenko, M., Griesfeller, A., Barret, B., LeFlochmoën, E., Clerbaux, C., Hadji-  
760 Lazaro, J., Coheur, P.F. and Hurtmans, D.: Validation of three different scientific ozone products  
761 retrieved from IASI spectra using ozonesondes, *Atmos. Meas. Tech.*, 5(3), pp.611-630, 2012.



762

763 Ebi, K.L. and McGregor, G., Climate change, tropospheric ozone and particulate matter, and health  
764 impacts, *Environmental health perspectives*, 116(11), pp.1449-1455, 2008.

765

766 Fadnavis, S., Dhomse, S., Ghude, S., Iyer, U., Buchunde, P., Sonbawne, S. and Raj, P.E.: Ozone  
767 trends in the vertical structure of Upper Troposphere and Lower stratosphere over the Indian  
768 monsoon region, *International Journal of Environmental Science and Technology*, 11(2), pp.529-  
769 542, 2014.

770

771 Fishbein, E., Farmer, C.B., Granger, S.L., Gregorich, D.T., Gunson, M.R., Hannon, S.E.,  
772 Hofstadter, M.D., Lee, S.Y., Leroy, S.S. and Strow, L.L.: Formulation and validation of simulated  
773 data for the Atmospheric Infrared Sounder (AIRS), *IEEE Transactions on Geoscience and Remote  
774 Sensing*, 41(2), pp.314-329, 2003.

775

776 Foret, G., Eremenko, M., Cuesta, J., Sellitto, P., Barré, J., Gaubert, B., Coman, A., Dufour, G.,  
777 Liu, X., Joly, M. and Doche, C.: Ozone pollution: What can we see from space? A case study, *J.  
778 Geophys. Res. Atmos.*, 119(13), pp.8476-8499, 2014.

779

780 Forster, P.M., Bodeker, G., Schofield, R., Solomon, S. and Thompson, D.: Effects of ozone cooling  
781 in the tropical lower stratosphere and upper troposphere, *Geophysical Research Letters*, 34(23),  
782 2007.

783



784 Finlayson-Pitts, B.J. and Pitts, J.N.: Tropospheric air pollution: ozone, airborne toxics, polycyclic  
785 aromatic hydrocarbons, and particles, *Science*, 276(5315), pp.1045-1051, 1997.  
786

787 Fishman, J., Ramanathan, V., Crutzen, P.J. and Liu, S.C.: Tropospheric ozone and climate, *Nature*,  
788 282(5741), pp.818-820, 1979.  
789

790 Fishman, J., Minnis, P. and Reichle Jr, H.G.: Use of satellite data to study tropospheric ozone in  
791 the tropics, *J. Geophys. Res. Atmos.*, 91(D13), pp.14451-14465, 1986.  
792

793 Fishman, J. and Larsen, J.C.: Distribution of total ozone and stratospheric ozone in the tropics:  
794 Implications for the distribution of tropospheric ozone, *J. Geophys. Res. Atmos.*, 92(D6), pp.6627-  
795 6634, 1987.  
796

797 Gautam, R., Hsu, N.C., Tsay, S.C., Lau, K.M., Holben, B., Bell, S., Smirnov, A., Li, C., Hansell,  
798 R., Ji, Q. and Payra, S.: Accumulation of aerosols over the Indo-Gangetic plains and southern  
799 slopes of the Himalayas: distribution, properties and radiative effects during the 2009 pre-monsoon  
800 season, *Atmos. Chem. Phys.*, 11(24), pp.12841-12863, 2011.  
801

802 Gauss, M., Myhre, G., Pitari, G., Prather, M.J., Isaksen, I.S.A., Berntsen, T.K., Brasseur, G.P.,  
803 Dentener, F.J., Derwent, R.G., Hauglustaine, D.A. and Horowitz, L.W.: Radiative forcing in the  
804 21st century due to ozone changes in the troposphere and the lower stratosphere, *J. Geophys. Res.*  
805 *Atmos.*, 108(D9), 2003.  
806



807 Hauglustaine, D.A. and Brasseur, G.P.: Evolution of tropospheric ozone under anthropogenic  
808 activities and associated radiative forcing of climate, *J. Geophys. Res. Atmos.*, 106(D23),  
809 pp.32337-32360, 2001.

810

811 Hudson, R.D. and Thompson, A.M.: Tropical tropospheric ozone from total ozone mapping  
812 spectrometer by a modified residual method, *J. Geophys. Res. Atmos.*, 103(D17), pp.22129-  
813 22145, 1998.

814

815 Heglin, M. I., Fahey, D. W., McFarland, M., Montzka, S. A., and Nash, E. R.: Twenty questions  
816 and answers about the ozone layer: 2014 update, *Scientific Assessment of Ozone Depletion: 2014*,  
817 84 pp., World Meteorological Organization, Geneva, Switzerland, ISBN 978-9966-076-02-1,  
818 2015.

819

820 Kim, J.H. and Newchurch, M.J.: Climatology and trends of tropospheric ozone over the eastern  
821 Pacific Ocean: The influences of biomass burning and tropospheric dynamics, *Geophysical*  
822 *research letters*, 23(25), pp.3723-3726, 1996.

823

824 Kim, J.H. and Newchurch, M.J.: Biomass- burning influence on tropospheric ozone over New  
825 Guinea and South America, *J. Geophys. Res. Atmos.*, 103(D1), pp.1455-1461, 1998.

826

827 Komhyr, W.D., Barnes, R.A., Brothers, G.B., Lathrop, J.A. and Opperman, D.P.: Electrochemical  
828 concentration cell ozonesonde performance evaluation during STOIC 1989, *J. Geophys. Res.*  
829 *Atmos.*, 100(D5), pp.9231-9244, 1995.



830

831 Komhyr, W.D.: Nonreactive gas sampling pump. *Review of Scientific Instruments*, 38(7), pp.981-  
832 983, 1967.

833

834 Kumar, R., Naja, M., Pfister, G.G., Barth, M.C. and Brasseur, G.P.: Simulations over South Asia  
835 using the Weather Research and Forecasting model with Chemistry (WRF-Chem): set-up and  
836 meteorological evaluation, *Geoscientific Model Development*, 5(2), pp.321-343, 2012a.

837

838 Kumar, R., Naja, M., Pfister, G.G., Barth, M.C., Wiedinmyer, C. and Brasseur, G.P.: Simulations  
839 over South Asia using the Weather Research and Forecasting model with Chemistry (WRF-  
840 Chem): chemistry evaluation and initial results, *Geoscientific Model Development*, 5(3), pp.619-  
841 648, 2012b.

842

843 Lacis, A.A., Wuebbles, D.J. and Logan, J.A.: Radiative forcing of climate by changes in the  
844 vertical distribution of ozone, *J. Geophys. Res. Atmos.*, 95(D7), pp.9971-9981, 1990.

845

846 Lal S., S. Venkataramani, S. Srivastava, S. Gupta, M. Naja, T. Sarangi, X. Liu.: Transport effects  
847 on the vertical distribution of tropospheric ozone over the tropical marine regions surrounding  
848 India, *J. Geophys. Res.*, 118, 1513-1524, doi:10.1002/jgrd.50180, 2013.

849

850 Lal S. S. Venkataramani, N. Chandra, O. R. Cooper, J. Brioude, and M. Naja, Transport effects on  
851 the vertical distribution of tropospheric ozone over western India, *J. Geophys. Res. Atmos.*, 119,  
852 doi:10.1002/2014JD021854, 2014.



853

854 Lal, S., Venkataramani, S., Naja, M., Kuniyal, J.C., Mandal, T.K., Bhuyan, P.K., Kumari, K.M.,  
855 Tripathi, S.N., Sarkar, U., Das, T. and Swamy, Y.V.: Loss of crop yields in India due to surface  
856 ozone: An estimation based on a network of observations, *Environmental Science and Pollution*  
857 *Research*, 24(26), pp.20972-20981, 2017.

858

859 Lawrence, M.G. and Lelieveld, J.: Atmospheric pollutant outflow from southern Asia: a review,  
860 *Atmospheric Chemistry and Physics*, 10(22), pp.11017-11096, 2010.

861

862 Lelieveld, J., Haines, A. and Pozzer, A.: Age-dependent health risk from ambient air pollution: a  
863 modelling and data analysis of childhood mortality in middle-income and low-income countries,  
864 *The lancet Planetary health*, 2(7), pp.e292-e300, 2018.

865

866 Logan, J.A.: Tropospheric ozone: Seasonal behavior, trends, and anthropogenic influence, *J.*  
867 *Geophys. Res. Atmos.*, 90(D6), pp.10463-10482, 1985.

868

869 Maddy, E.S. and Barnet, C.D.: Vertical resolution estimates in version 5 of AIRS operational  
870 retrievals, *IEEE Transactions on Geoscience and Remote Sensing*, 46(8), pp.2375-2384, 2008.

871

872 McPeters, R.D., Miles, T., Flynn, L.E., Wellemeyer, C.G. and Zawodny, J.M.: Comparison of  
873 SBUV and SAGE II ozone profiles: Implications for ozone trends, *J. Geophys. Res. Atmos.*,  
874 99(D10), pp.20513-20524, 1994.

875



876 McPeters, R.D., Labow, G.J. and Johnson, B.J.: A satellite- derived ozone climatology for  
877 balloonsonde estimation of total column ozone, *J. Geophys. Res. Atmos.*, 102(D7), pp.8875-8885,  
878 1997.

879

880 McPeters, R.D., Labow, G.J. and Logan, J.A.: Ozone climatological profiles for satellite retrieval  
881 algorithms, *J. Geophys. Res. Atmos.*, 112(D5), 2007.

882

883 Monahan, K.P., Pan, L.L., McDonald, A.J., Bodeker, G.E., Wei, J., George, S.E., Barnet, C.D. and  
884 Maddy, E.: Validation of AIRS v4 ozone profiles in the UTLS using ozonesondes from Lauder,  
885 NZ and Boulder, USA, *J. Geophys. Res. Atmos.*, 112(D17), 2007.

886

887 Munro, R., Siddans, R., Reburn, W.J. and Kerridge, B. J.: Direct measurement of tropospheric  
888 ozone distributions from space, *Nature*, 392(6672), pp.168-171, 1998.

889

890 Naja, M., C Mallik, T. Sarangi, V Sheel, S. Lal, SO<sub>2</sub> measurements at a high altitude site in the  
891 central Himalayas: Role of regional transport, *Atmospheric Environment*,  
892 doi:10.1016/j.atmosenv.2014.08.031, 2014.

893

894 Naja M., Piyush Bhardwaj, N. Singh, Phani Kumar, R. Kumar, N. Ojha, Ram Sagar, S. K.  
895 Satheesh, K. Krishna Moorthy and V. R. Kotamarthi: High-frequency vertical profiling of  
896 meteorological parameters using AMF1 facility during RAWEX–GVAX at ARIES, Nainital,  
897 *Current Science*, vol 111, issue 1, 2016.

898



899 Nalli, N.R., Barnet, C.D., Reale, A., Tobin, D., Gambacorta, A., Maddy, E.S., Joseph, E., Sun, B.,  
900 Borg, L., Mollner, A.K. and Morris, V.R.: Validation of satellite sounder environmental data  
901 records: Application to the Cross-track Infrared Microwave Sounder Suite, *J. Geophys. Res.*  
902 *Atmos.*, 118(24), pp.13-628, 2013.

903

904 Nalli, N.R., Gambacorta, A., Liu, Q., Tan, C., Iturbide-Sanchez, F., Barnet, C.D., Joseph, E.,  
905 Morris, V.R., Oyola, M. and Smith, J.W.: Validation of Atmospheric Profile Retrievals from the  
906 SNPP NOAA-Unique Combined Atmospheric Processing System. Part 2: Ozone, *IEEE*  
907 *Transactions on Geoscience and Remote Sensing*, 56(1), pp.598-607, 2017.

908

909 Oltmans, S.J.: Surface ozone measurements in clean air, *J. Geophys. Res. Oceans*, 86(C2),  
910 pp.1174-1180, 1981.

911

912 Oltmans, S.J. and Komhyr, W.D.: Surface ozone distributions and variations from 1973–1984:  
913 Measurements at the NOAA Geophysical Monitoring for Climatic Change Baseline  
914 Observatories, *J. Geophys. Res. Atmos.*, 91(D4), pp.5229-5236, 1986.

915

916 Ojha, N., Naja, M., Sarangi, T., Kumar, R., Bhardwaj, P., Lal, S., Venkataramani, S., Sagar, R.,  
917 Kumar, A. and Chandola, H.C.: On the processes influencing the vertical distribution of ozone  
918 over the central Himalayas: Analysis of yearlong ozonesonde observations, *Atmospheric*  
919 *Environment*, 88, pp.201-211, 2014.

920





921 Oltmans, S.J., Hofmann, D.J., Lathrop, J.A., Harris, J.M., Komhyr, W.D. and Kuniyuki, D.:  
922 Tropospheric ozone during Mauna Loa Observatory Photochemistry Experiment 2 compared to  
923 long- term measurements from surface and ozonesonde observations, *J. Geophys. Res. Atmos.*,  
924 101(D9), pp.14569-14580, 1996.

925

926 Oltmans, S.J., Lefohn, A.S., Harris, J.M. and Shadwick, D.S.: Background ozone levels of air  
927 entering the west coast of the US and assessment of longer-term changes. *Atmospheric*  
928 *Environment*, 42(24), pp.6020-6038, 2008.

929

930 Pagano, T.S., Aumann, H.H., Hagan, D.E. and Overoye, K.: Prelaunch and in-flight radiometric  
931 calibration of the Atmospheric Infrared Sounder (AIRS), *IEEE transactions on geoscience and*  
932 *remote sensing*, 41(2), pp.265-273, 2003.

933

934 Pierce, R.B., Al- Saadi, J., Kittaka, C., Schaack, T., Lenzen, A., Bowman, K., Szykman, J., Soja,  
935 A., Ryerson, T., Thompson, A.M. and Bhartia, P.: Impacts of background ozone production on  
936 Houston and Dallas, Texas, air quality during the Second Texas Air Quality Study field mission,  
937 *J. Geophys. Res. Atmos.*, 114(D7), 2009.

938

939 Pittman, J.V., Pan, L.L., Wei, J.C., Irion, F.W., Liu, X., Maddy, E.S., Barnet, C.D., Chance, K.  
940 and Gao, R.S.: Evaluation of AIRS, IASI, and OMI ozone profile retrievals in the extratropical  
941 tropopause region using in situ aircraft measurements, *J. Geophys. Res. Atmos.*, 114(D24), 2009.

942



- 943 Qu, Z.W., Zhu, H., Grebenshchikov, S.Y., Schinke, R. and Farantos, S.C.: The Huggins band of  
944 ozone: A theoretical analysis, *The Journal of chemical physics*, 121(23), pp.11731-11745, 2004.  
945
- 946 Rawat, P., Naja, M., Thapliyal, P.K., Srivastava, S., Bhardwaj, P., Kumar, R., Bhattacharjee, S.,  
947 Venkatramani, S., Tiwari, S.N. and Lal, S.: Assessment of vertical ozone profiles from INSAT-  
948 3D sounder over the Central Himalaya. *Current Science*, 119(7), p.1113, 2020.
- 949 Rawat, P. and Naja, M.: Remote sensing study of ozone, NO<sub>2</sub>, and CO: some contrary effects of  
950 SARS-CoV-2 lockdown over India. *Environ Sci Pollut Res*, [https://doi.org/10.1007/s11356-021-](https://doi.org/10.1007/s11356-021-17441-2)  
951 17441-2, 2021.
- 952 Sarangi T., M. Naja, N. Ojha, R. Kumar, S. Lal, S. Venkataramani, A. Kumar, R. Sagar and H. C.  
953 Chandola: First simultaneous measurements of ozone, CO and NO<sub>y</sub> at a high altitude regional  
954 representative site in the central Himalayas, *J. Geophys. Res.*, 119, doi:10.1002/2013JD020631,  
955 2014.  
956
- 957 Seemann, S.W., Li, J., Menzel, W.P. and Gumley, L.E.: Operational retrieval of atmospheric  
958 temperature, moisture, and ozone from MODIS infrared radiances, *Journal of applied*  
959 *meteorology*, 42(8), pp.1072-1091, 2003.  
960
- 961 Shindell, D., Kuylenstierna, J.C., Vignati, E., van Dingenen, R., Amann, M., Klimont, Z.,  
962 Anenberg, S.C., Muller, N., Janssens-Maenhout, G., Raes, F. and Schwartz, J.: Simultaneously  
963 mitigating near-term climate change and improving human health and food security, *Science*,  
964 335(6065), pp.183-189, 2012.  
965



966 Smit, H.G., Straeter, W., Johnson, B.J., Oltmans, S.J., Davies, J., Tarasick, D.W., Hoegger, B.,  
967 Stubi, R., Schmidlin, F.J., Northam, T. and Thompson, A.M.: Assessment of the performance of  
968 ECC- ozonesondes under quasi- flight conditions in the environmental simulation chamber:  
969 Insights from the Juelich Ozone Sonde Intercomparison Experiment (JOSIE), *Journal of*  
970 *Geophysical Research: Atmospheres*, 112(D19), 2007.

971

972 Srivastava S., Manish Naja, V. Thouret: Influences of regional pollution and long range transport  
973 over Hyderabad using ozone data from MOZAIC, *Atmospheric Environment*, 117, pp.135-146,  
974 2015.

975

976 Stevenson, D.S., Young, P.J., Naik, V., Lamarque, J.F., Shindell, D.T., Voulgarakis, A., Skeie,  
977 R.B., Dalsoren, S.B., Myhre, G., Bernsten, T.K. and Folberth, G.A.: Tropospheric ozone changes,  
978 radiative forcing and attribution to emissions in the Atmospheric Chemistry and Climate Model  
979 Intercomparison Project (ACCMIP), *Atmos. Chem. Phys.*, 13(6), pp.3063-3085, 2013.

980

981 Susskind, J., Barnet, C.D. and Blaisdell, J.M.: Retrieval of atmospheric and surface parameters  
982 from AIRS/AMSU/HSB data in the presence of clouds, *IEEE Transactions on Geoscience and*  
983 *Remote Sensing*, 41(2), pp.390-409, 2003.

984

985 Susskind, J., Barnet, C., Blaisdell, J., Iredell, L., Keita, F., Kouvaris, L., Molnar, G. and Chahine,  
986 M.: Accuracy of geophysical parameters derived from Atmospheric Infrared Sounder/Advanced  
987 Microwave Sounding Unit as a function of fractional cloud cover, *J. Geophys. Res. Atmos.*,  
988 111(D9), 2006.



989

990 Veefkind, J.P., de Haan, J.F., Brinksma, E.J., Kroon, M. and Levelt, P.F.: Total ozone from the  
991 Ozone Monitoring Instrument (OMI) using the DOAS technique, IEEE transactions on geoscience  
992 and remote sensing, 44(5), pp.1239-1244, 2006.

993

994 Verstraeten, W. W., Boersma, K. F., Zörner, J., Allaart, M. A. F., Bowman, K. W., and Worden,  
995 J. R.: Validation of six years of TES tropospheric ozone retrievals with ozonesonde measurements:  
996 implications for spatial patterns and temporal stability in the bias, Atmos. Meas. Tech., 6, 1413–  
997 1423, <https://doi.org/10.5194/amt-6-1413-2013>, 2013.

998

999 Wang, W.C., Pinto, J.P. and Yung, Y.L.: Climatic effects due to halogenated compounds in the  
1000 Earth's atmosphere. Journal of Atmospheric Sciences, 37(2), pp.333-338, 1980.

1001

1002 Wang, W.C., Zhuang, Y.C. and Bojkov, R.D.: Climate implications of observed changes in ozone  
1003 vertical distributions at middle and high latitudes of the Northern Hemisphere, Geophysical  
1004 research letters, 20(15), pp.1567-1570, 1993.

1005

1006 Wang, B., R. Wu, K.-M. Lau: Interannual variability of Asian summer monsoon: Contrast between  
1007 the Indian and western North Pacific-East Asian monsoons. J. Climate, 14, 4073-4090, 2001.

1008

1009 Wang, W., Cheng, T., van der A, R.J., de Laat, J. and Williams, J.E.: Verification of the  
1010 Atmospheric Infrared Sounder (AIRS) and the Microwave Limb Sounder (MLS) ozone algorithms  
1011 based on retrieved daytime and night-time ozone, Atmos. Meas. Tech., 14(2), pp.1673-1687, 2021.



1012

1013 Zhu, T., W. Lin, Y. Song, X. Cai, H. Zou, L. Kang, L. Zhou, and H. Akimoto: Downward transport  
1014 of ozone-rich air near Mt. Everest, *Geophys. Res. Lett.*, 33, L23809, doi:10.1029/2006GL027726,  
1015 2006.

1016

1017 Ziemke, J.R., Chandra, S. and Bhartia, P. K.: Two new methods for deriving tropospheric column  
1018 ozone from TOMS measurements: Assimilated UARS MLS/HALOE and convective- cloud  
1019 differential techniques, *J. Geophys. Res. Atmos.*, 103(D17), pp.22115-22127, 1998.

1020

1021 Ziemke, J.R., Chandra, S., Duncan, B.N., Froidevaux, L., Bhartia, P.K., Levelt, P.F. and Waters,  
1022 J.W.: Tropospheric ozone determined from Aura OMI and MLS: Evaluation of measurements and  
1023 comparison with the Global Modeling Initiative's Chemical Transport Model, *J. Geophys. Res.*  
1024 *Atmos.*, 111(D19), 2006.

1025

1026

1027

1028

1029

1030

1031

1032

1033

1034



1035 **Table 1.** Ozone mixing ratio (ppbv) from ozonesonde, ozonesonde(AK) and AIRS over Nainital  
 1036 at six pressure levels and during winter, spring, summer-monsoon, autumn. The number of  
 1037 ozonesonde flights during four seasons are mentioned in the bracket.

Pressure levels		706 (hPa)	496 (hPa)	300 (hPa)	103 (hPa)	29 (hPa)	14.4 (hPa)
Winter (61)	ozonesonde	55.1±7.3	54.4±5.9	69.5±21.4	238.8±116.7	4569.3±524.4	7620.6±1105
	ozonesonde (AK)	48.6±3.4	55.9±4.7	70.4±14.2	187.3±29.1	5249.1±634.1	8214.9±862.1
	AIRS	46.5±3.1	52.2±5.2	68.7±9.3	354.4±63.4	4428.2±456.9	6616.4±447.4
Spring (72)	ozonesonde	71.6±11.6	70.2±11.5	81.5±18.6	223.9±99.3	4747.0±339.6	8242.3±827.0
	ozonesonde (AK)	58.7±5.0	69.1±6.8	80.3±11.3	221.8±30.1	5137.8±532.7	8784.4±790.7
	AIRS	55.3±2.8	60.7±4.9	78.6±8.2	389.2±46.6	4687.4±314.2	7852.4±395.5
Summer- monsoon (55)	ozonesonde	53.0±11.8	65.1±15.7	82.1±17.4	138.6±24.2	4642.9±193.2	8493.6±709.4
	ozonesonde (AK)	44.1±5.7	62.3±9.3	68.7±10.6	224.3±13.8	5271.3±322.3	9233.8±527.8
	AIRS	48.8±1.4	57.5±2.1	63.6±2.6	267.4±18.9	4710.0±363.0	8333.1±577.0
Autumn (54)	ozonesonde	53.0±8.0	63.8±11.1	72.7±9.7	144.6±41.2	4439.3±195.9	8613.7±616.0
	ozonesonde (AK)	50.4±4.0	61.0±5.5	64.1±6.4	169.0±8.3	5086.3±242.0	9035.8±398.0
	AIRS	46.0±1.6	51.3±2.7	56.9±3.5	241.8±21.1	4635.4±277.0	7984.9±465.0

1038

1039

1040

1041



1042 **Table 2.** Coefficient of determination ( $r^2$ ) of three IR satellite sensors (AIRS, IASI and CrIS) ozone  
1043 retrieval in four broad layers with respect to ozonesonde observations.

	Coefficient of determination ( $r^2$ )		
	AIRS	IASI	CrIS
600 - 800 hPa	0.52	0.34	0.09
300 - 600 hPa	0.44	0.31	0.22
100 - 300 hPa	0.45	0.44	0.45
10 - 100 hPa	0.97	0.91	0.98

1044

1045

1046

1047 **Table 3.** Total column ozone (TCO) differences in DU between AIRS, OMI and ozonesonde (AK),  
1048 during twelve months.

TCO Diff. (DU)	Jan	Feb	Mar	Apr	May	Jun	Jul	Aug	Sep	Oct	Nov	Dec
AIRS-OMI	-3.9	2.2	-1.8	13.2	16.7	18	-2.2	17.2	22.1	13.2	0.0	-2.7
AIRS- ozonesonde (AK)	-6.7	2.2	-2.3	6.5	17.3	13	-3.1	20.3	19.1	10.3	0.2	-10.7

1049

1050

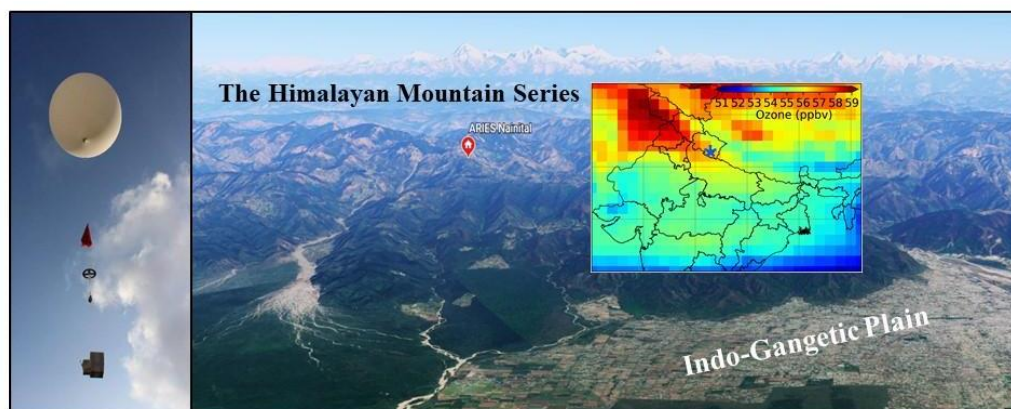
1051

1052

1053



1054



1055

1056 **Figure 1.** Location (red color circle) of the balloon launching site (Map from © Google Earth, 2021)  
1057 situated in the Aryabhata Research Institute of Observational Sciences (ARIES) ( $29.4^{\circ}$  N,  $79.5^{\circ}$   
1058 E, and 1793 m elevation), Nainital in the central Himalaya. The spatial distribution of ozone  
1059 (AIRS) at 500 hPa is also shown over northern India and the location of the site is marked with a  
1060 blue star. A photo of balloon, together with parachute, unwinder, ozonesonde along with GPS-  
1061 radiosonde above the observation site is also shown at the left.

1062

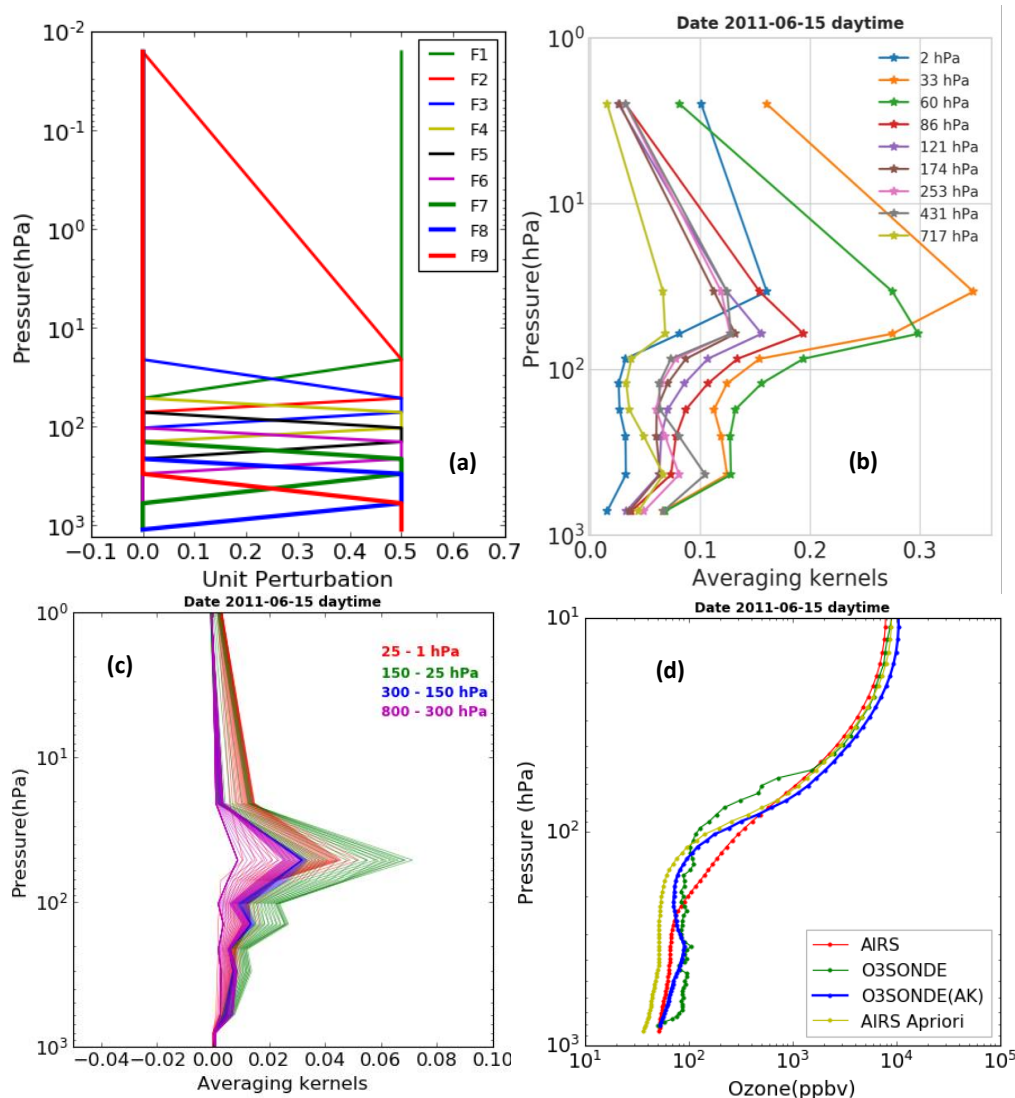
1063

1064

1065

1066



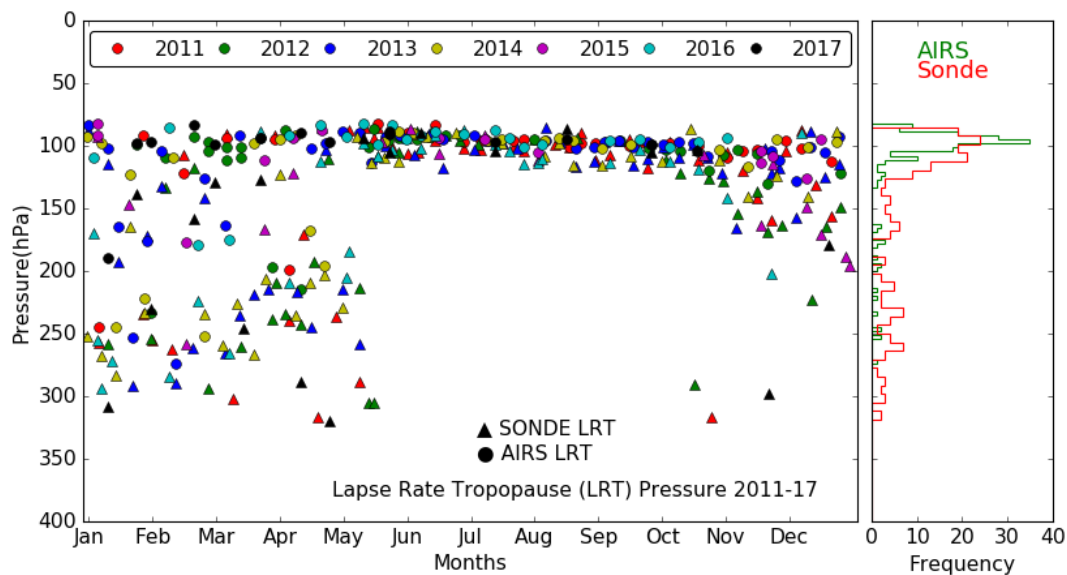


1067

1068

1069

1070 **Figure 2.** (a) Nine trapezoid functions used for ozone retrieval in AIRS-V6. (b) AIRS ozone  
 1071 averaging kernel matrix over Nainital at 9 levels vertical grid. (c) Calculated AIRS averaging  
 1072 kernel matrices at 100 RTA grids after applying the trapezoid function. (d) An example of ozone  
 1073 profiles using different data sets for 15 Jun 2011 over the observation site.



1074

1075 **Figure 3.** Lapse rate tropopause pressure monthly variation from balloon-borne and AIRS  
1076 observations and respective frequency distributions during 2011 - 2017.

1077

1078

1079

1080

1081

1082

1083

1084

1085

1086

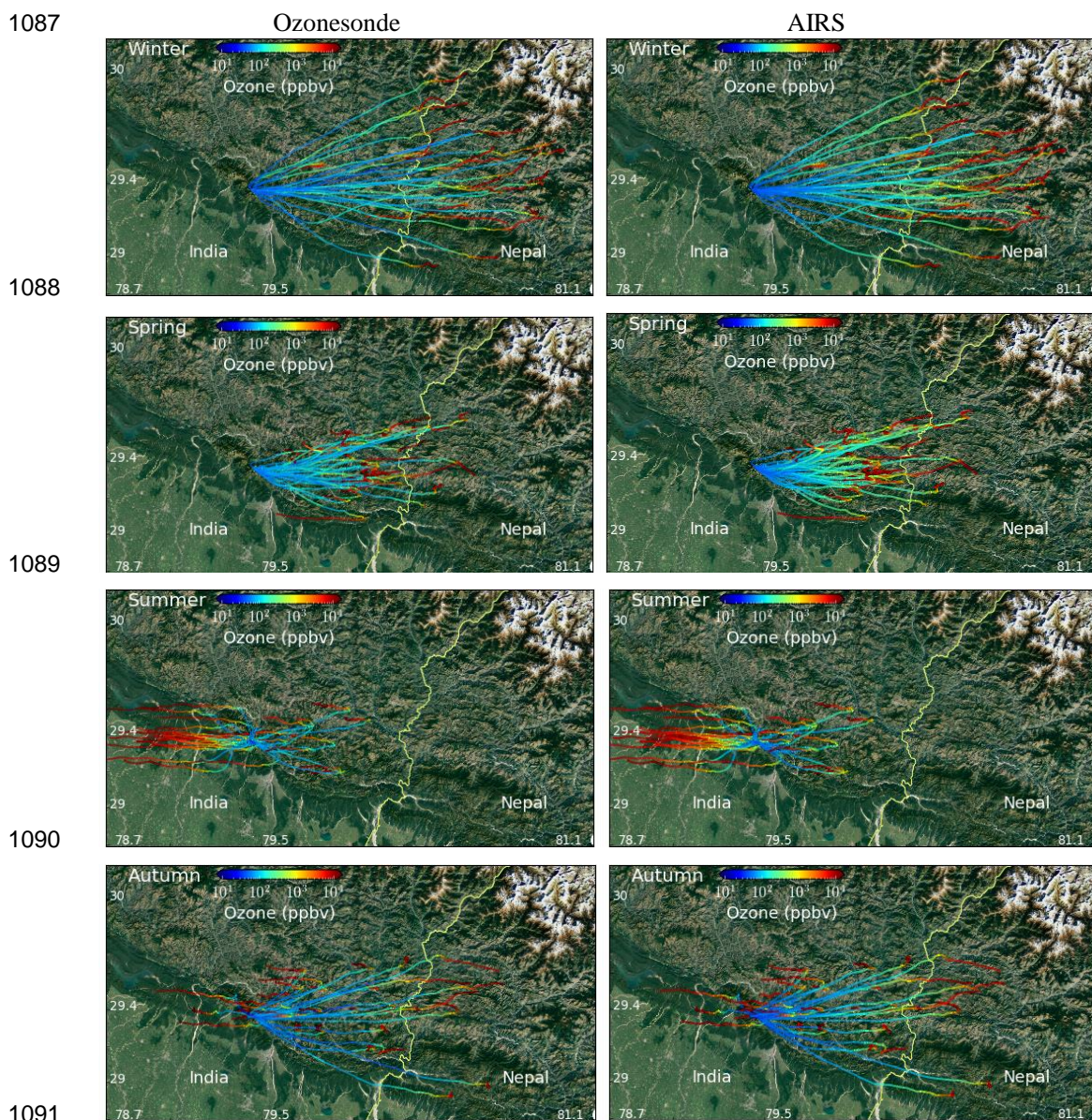
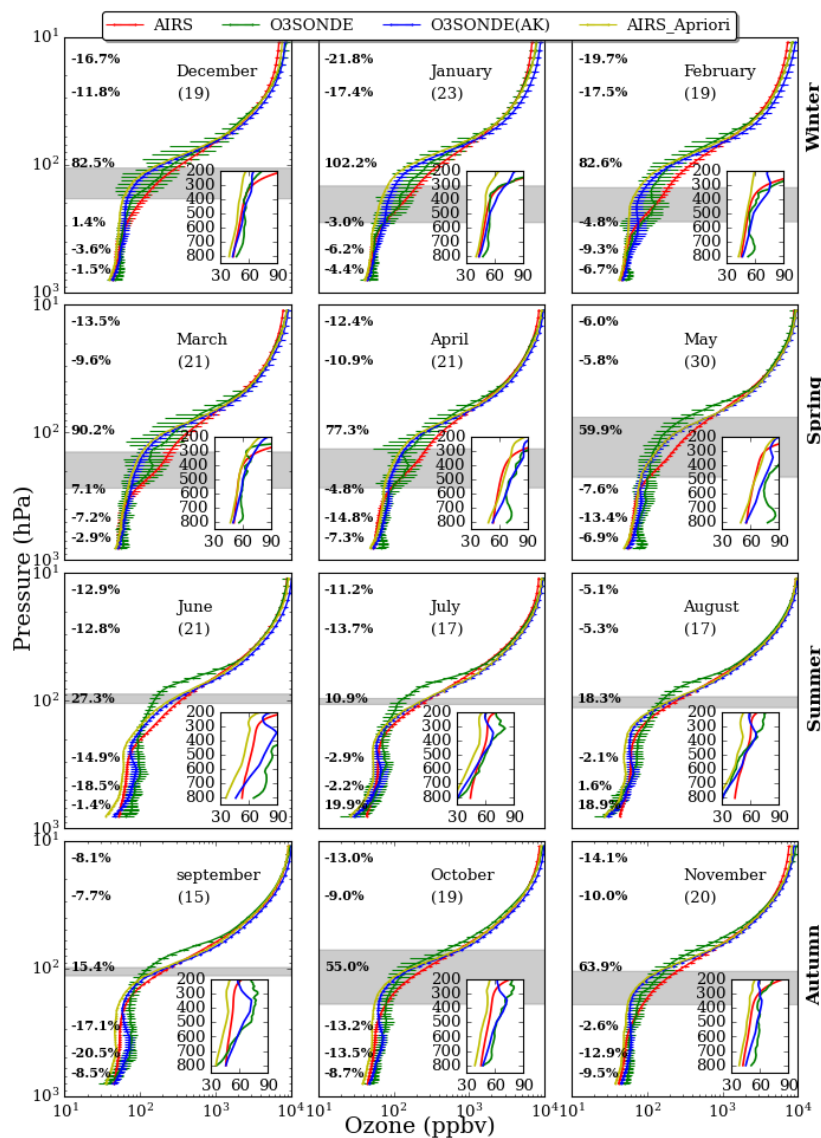
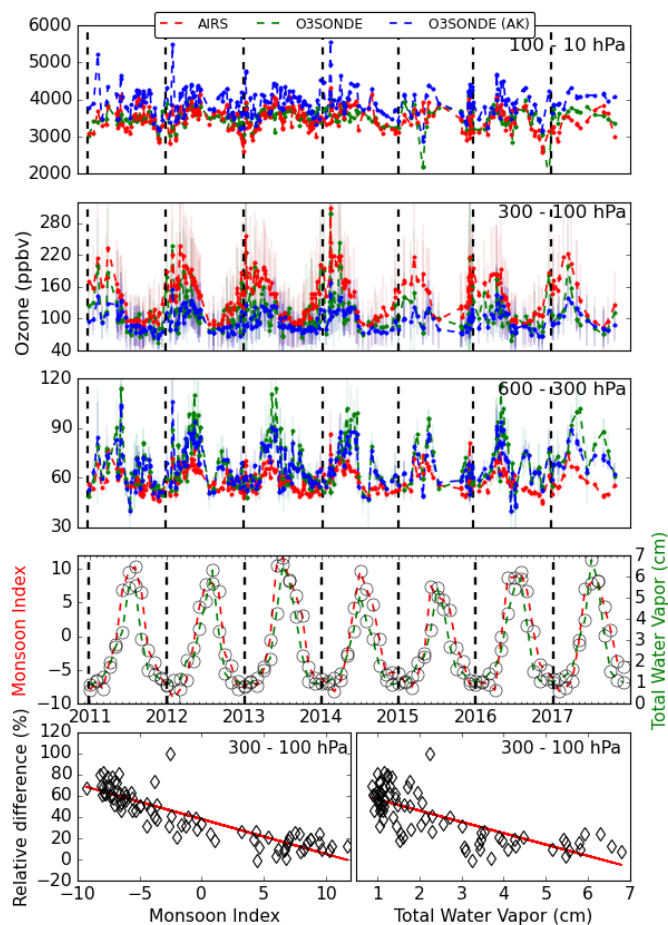


**Figure 4.** Spatial distribution of ozone using all ozone sounding (left) launched from ARIES, Nainital, India (Map from © Google Earth, 2021). Ozone spatial distribution from AIRS (right), following the balloon track, is also shown. It could be seen that the balloon reaches Nepal many times in the winter and autumn seasons.



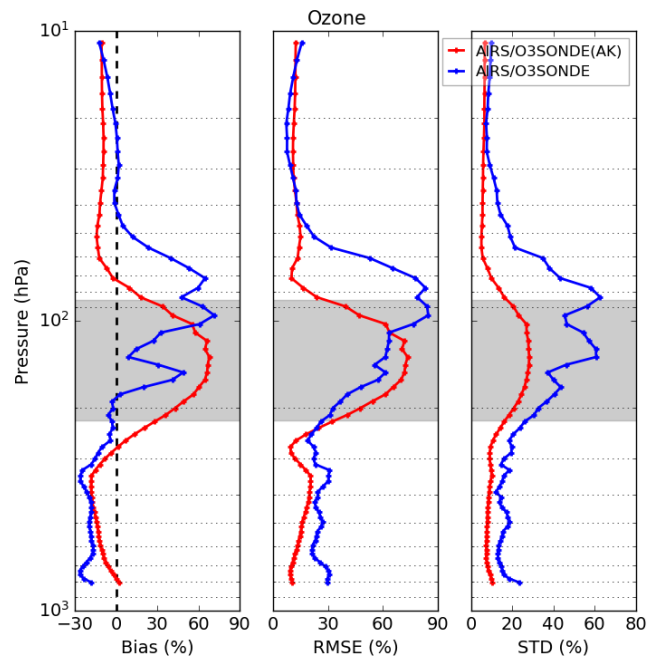
1098

1099 **Figure 5.** Monthly averaged (2011-2017) ozone profiles of ozonesonde, AIRS, ozonesonde(AK)  
 1100 and AIRS a-priori over Nainital in the central Himalaya. The percentage difference  $[(\text{AIRS} -$   
 1101  $\text{ozonesonde(AK)})/\text{ozonesonde(AK)}] \times 100$  at 706, 496, 300, 103, 29, and 14.4 hPa are also written  
 1102 at respective altitudes. The number of ozonesonde for different months is written in the bracket  
 1103 and grey shaded area shows the tropopause (mean $\pm$ sigma) from balloon-borne observations.



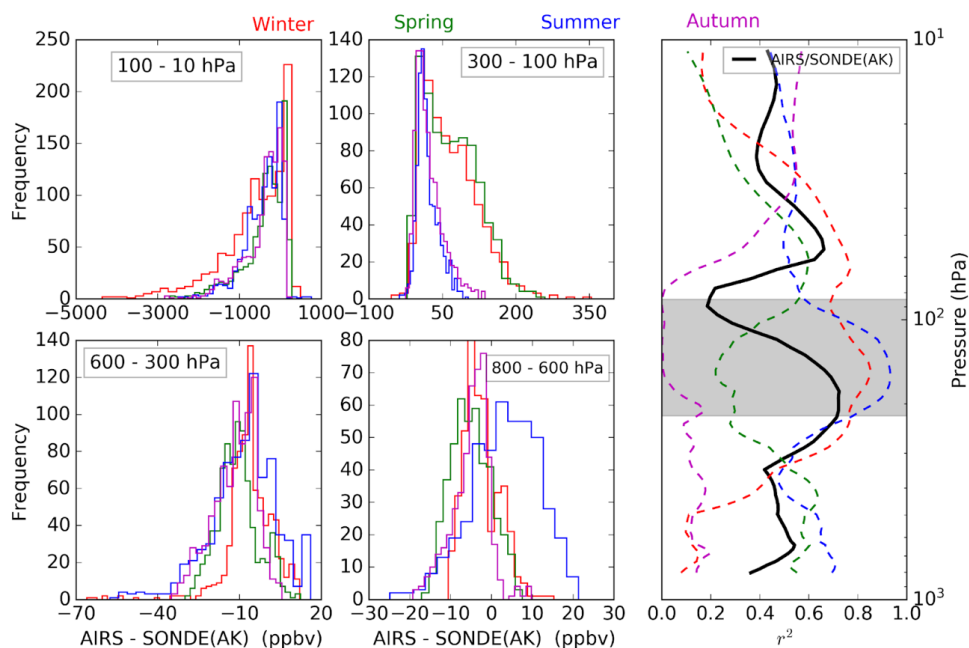
1104  
1105  
1106  
1107  
1108  
1109  
1110  
1111  
1112

**Figure 6.** Average variations in ozone mixing ratios at three defined layers, characterizing the lower/middle stratosphere (100 - 10 hPa), the upper troposphere (300 - 100 hPa), and the middle troposphere (600 - 300 hPa), respectively. The monthly variation of the total column water vapor (cm) along with the monsoon index is also shown. The scattered plot of ozone relative difference (%)  $[(AIRS-O3SONDE(AK))/O3SONDE(AK)]*100$ , with monsoon index and total water vapor in the upper troposphere (300 - 100 hPa) is also shown at the bottom.



1113

1114 **Figure 7.** Statistical error analysis of AIRS retrieved ozone with ozonesonde and ozonesonde (AK)  
1115 for collocated data of seven years (2011 - 2017). The grey shaded area shows the tropopause region  
1116 from balloon-borne observations.

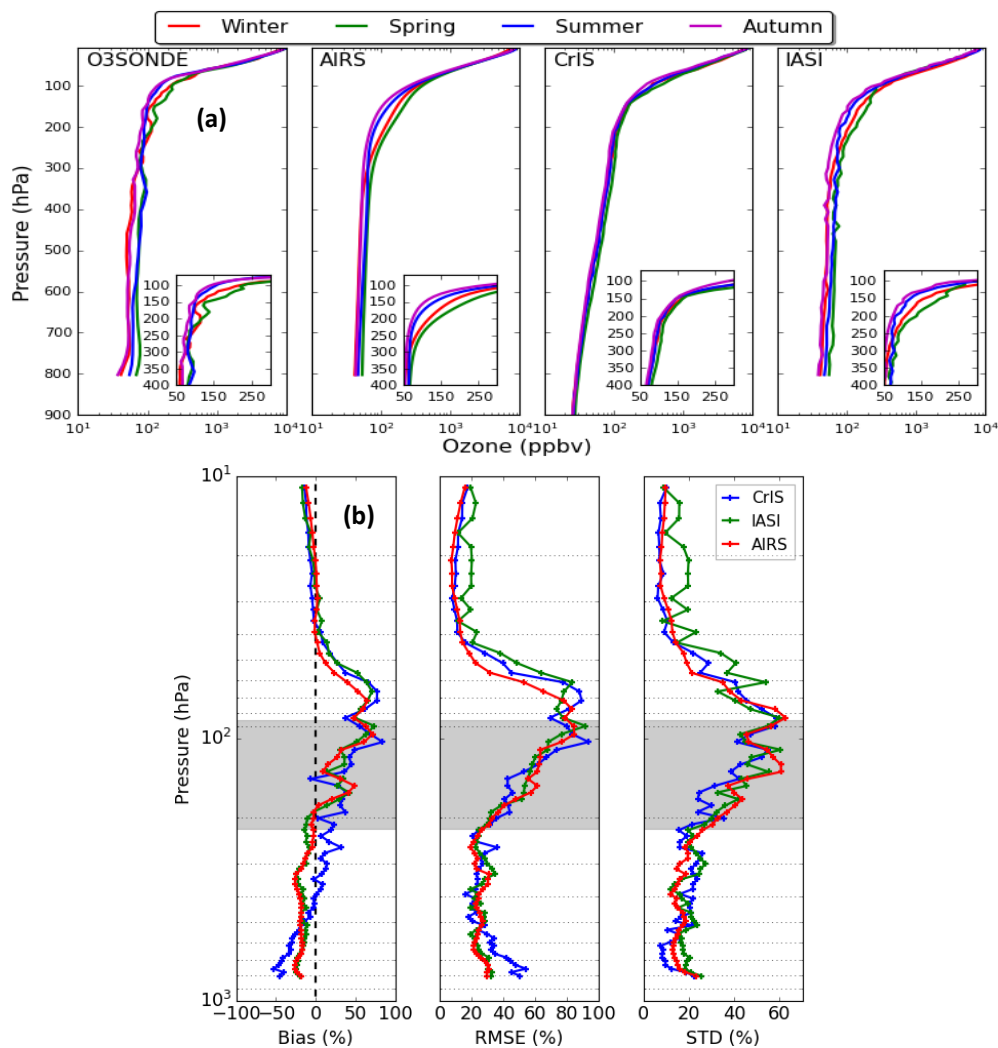


1117

1118 **Figure 8.** Histogram remainder between AIRS ozone and ozonesonde(AK) in the four defined  
1119 layers. The average correlation profile between AIRS ozone and ozonesonde(AK) is shown on the  
1120 right during winter (red), spring (green), summer-monsoon (blue), and autumn (magenta). The  
1121 black line is for the entire data set. The grey shaded area shows the tropopause region from balloon-  
1122 borne observations.

1123

1124

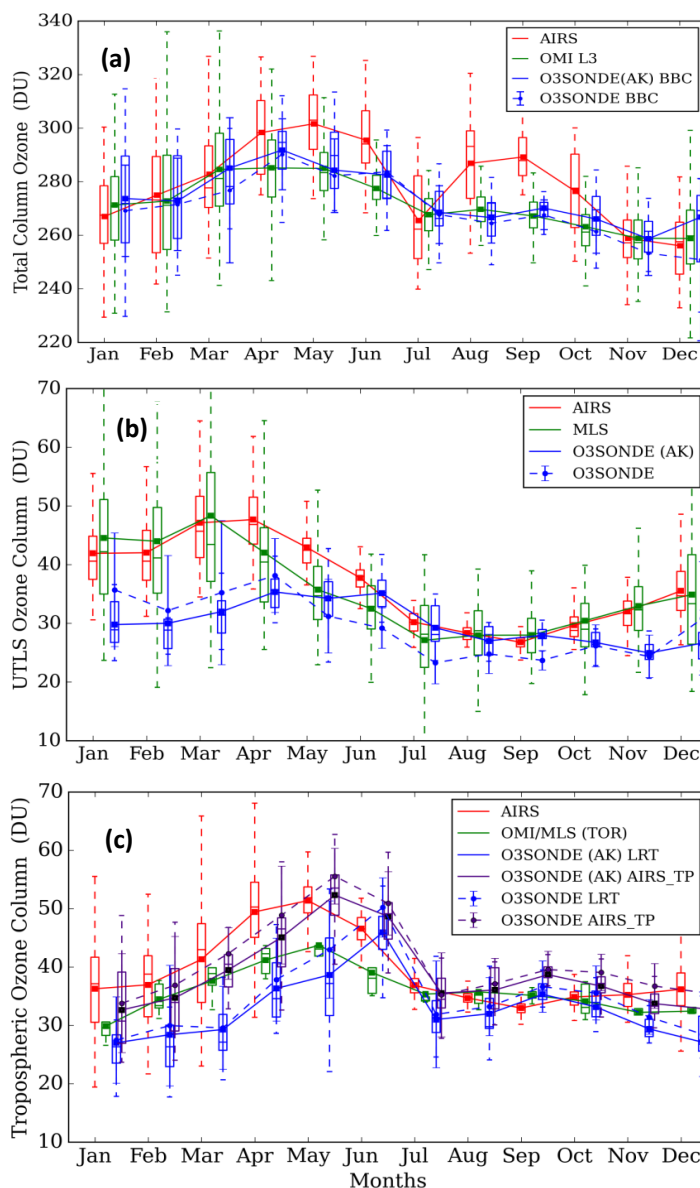


1125

1126

1127 **Figure 9.** (a) Seasonal ozone profiles of three IR satellites (IASI, AIRS, and CrIS) for a smaller  
1128 sample size (April 2014 to April 2015). The IASI and CrIS products are generated using the AIRS  
1129 heritage algorithm (NOAA) and only IR+MW successful retrieval was used in quality control  
1130 (QC=0). (b) Statistical error analysis for the three IR satellites retrieved ozone without applying  
1131 the averaging kernel information. The grey shaded area shows the tropopause region from balloon-  
1132 borne observations.





1133

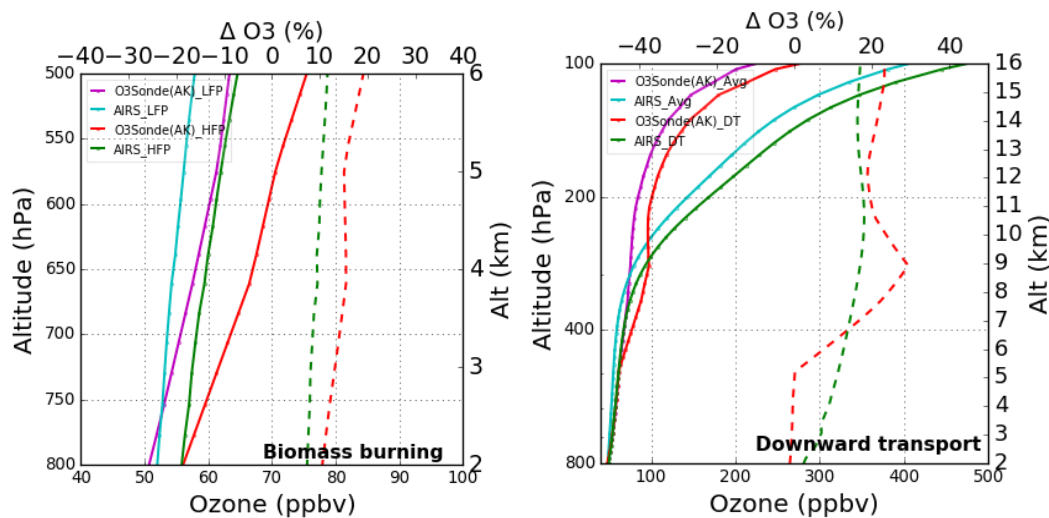
1134

1135

1136 **Figure 10.** (a) Monthly average variation of total column ozone (TCO) for AIRS, OMI, and  
1137 ozonesonde over the central Himalaya for the seven-year period (2011-2017). (b) Monthly average  
1138 variation of UTLS ozone column for AIRS, MLS, and ozonesonde, over the central Himalayas for  
1139 the seven-year periods (2011-2017). (c) Monthly average variation of tropospheric ozone column  
1140 of AIRS, OMI/MLS, and ozonesonde, over the central Himalayas for the seven-year periods  
1141 (2011-2017). The monthly average from ozonesonde is also shown while using AIRS tropopause.



1142



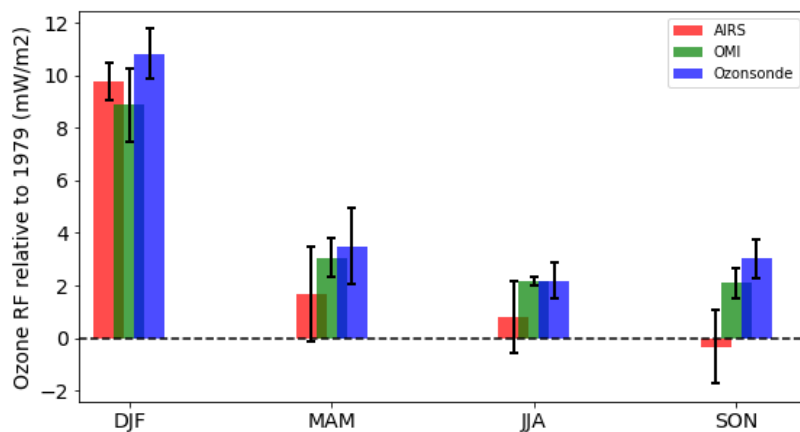
1143

1144 **Figure 11.** (a) Vertical ozone profiles of AIRS ozone and ozonesonde(AK) during low fire period  
1145 (LFP) and high fire period (HEP). The solid line corresponds to ozone profiles while the dotted  
1146 line shows a percentage increase in ozonesonde (red) and AIRS (green) profiles during biomass  
1147 burning events. (b) Vertical ozone profiles of AIRS ozone and ozonesonde(AK) during events of  
1148 downward transport. Dotted line shows ozone enhancement during downward transport events.

1149

1150

1151



1152

1153 **Figure 12.** Seasonal average ozone UV radiative forcing (RF) relative to 1979 as calculated from  
1154 ozonsonde, OMI, and AIRS total ozone data during the 2011 - 2017 period.

1155